



1 **Deciphering the metamorphic evolution of the Pulo do**  
2 **Lobo metasedimentary belt (SW Iberian Variscides)**

3

4 Irene Pérez-Cáceres<sup>1</sup>, David Jesús Martínez Poyatos<sup>1</sup>, Olivier Vidal<sup>2</sup>, Olivier Beyssac<sup>3</sup>,  
5 Fernando Nieto<sup>4</sup>, José Fernando Simancas<sup>1</sup>, Antonio Azor<sup>1</sup> and Franck Bourdelle<sup>5</sup>

6

7 1 Departamento de Geodinámica, Facultad de Ciencias, Universidad de Granada, Campus de  
8 Fuentenueva s/n, 18071 Granada, Spain.

9 2 Institut de Sciences de la Terre (ISTerre), CNRS-University of Grenoble 1, 1381 rue de la Piscine,  
10 38041 Grenoble, France.

11 3 Institut de Physique des Matériaux et de Cosmochimie (IMPMC), CNRS-Sorbonne Université,  
12 Case Courrier 115, 4 place Jussieu, 75005 Paris, France.

13 4 Departamento de Mineralogía y Petrología, IACT, Facultad de Ciencias, Universidad de Granada-  
14 CSIC, Campus de Fuentenueva s/n, 18071 Granada, Spain.

15 5 Laboratoire Génie Civil et géo-Environnement (LGCgE), Université de Lille, Bât. SN5, Cité  
16 Scientifique, 59655 Villeneuve d'Ascq, France

17 Correspondence to: Irene Pérez-Cáceres (perezcaceres@ugr.es)

18

19

20 **Abstract**

21 The Pulo do Lobo belt is one of the units related to the orogenic suture between the Ossa-  
22 Morena and the South Portuguese zones in the SW Iberian Variscides. This metasedimentary  
23 unit has been classically interpreted as a Rheic subduction-related accretionary prism formed  
24 during the pre-Carboniferous convergence and eventual collision between the South  
25 Portuguese Zone (part of Avalonia) and the Ossa-Morena Zone (peri-Gondwanan terrane).  
26 Discrete mafic intrusions also occur in the dominant Pulo do Lobo metapelites, related to  
27 an intraorogenic Mississippian transtensional and magmatic event that had a significant  
28 thermal input. Three different approaches have been applied to the  
29 Devonian/Carboniferous phyllites and slates of the Pulo do Lobo belt in order to study their  
30 poorly known low-grade metamorphic evolution. X-Ray diffraction (XRD) was used to  
31 unravel the mineralogy and measure crystallographic parameters (illite “crystallinity” and K-  
32 white mica *b*-cell dimension). Compositional maps of selected samples were obtained from  
33 electron probe microanalysis, which allowed processing with XmapTools software, and  
34 chlorite semi-empirical and thermodynamic geothermometry was performed. Thermometry



35 based on Raman spectroscopy of carbonaceous material (RSCM) was used to obtain peak  
36 temperatures.

37 The microstructural study shows the existence of two phyllosilicate growth events at the  
38 chlorite zone, the main one ( $M_1$ ) related to the development of a Devonian foliation  $S_1$ , and  
39 a minor one ( $M_2$ ) associated with a crenulation cleavage ( $S_2$ ) developed at middle/upper  
40 Carboniferous time.  $M_1$  entered well into epizone (greenschist facies) conditions.  $M_2$   
41 conditions were at lower temperature, reaching the anchizone/epizone boundary. These data  
42 accord well with the unconformity that separates the Devonian and Carboniferous  
43 formations of the Pulo do Lobo belt. The varied results obtained by the different approaches  
44 followed, combined with microstructural analysis, are indicative of different snapshots of the  
45 metamorphic history. Thus, RSCM temperatures are higher in comparison with the other  
46 methods applied, which is interpreted as reflecting a faster reequilibration during the short-  
47 lived thermal Mississippian event. Regarding the metamorphic pressure, the data are very  
48 homogeneous (very low celadonite content in muscovite and low values of K-white mica  $b$ -  
49 cell dimension), indicating a low-pressure gradient, which is unexpected in a subduction-  
50 related accretionary prism.

51

## 52 **Keywords**

53 Pulo do Lobo metapelites

54 Low-pressure gradient

55 X-Ray diffraction

56 Chlorite geothermometry

57 Raman spectroscopy of carbonaceous material

58

## 59 **Highlights**

60 A multidisciplinary approach has been applied to study the metamorphism of the Pulo do  
61 Lobo metapelites.

62 Devonian metamorphism entered epizone conditions.

63 Carboniferous metamorphism reached the anchizone/epizone boundary.

64 The inferred low-pressure gradient is incompatible with a subduction-related accretionary  
65 prism.



## 66 1. Introduction

67 The knowledge of temperature and pressure conditions reached by the low-grade  
68 metasedimentary units stacked hinterlands of orogens helps to better interpret their  
69 tectonometamorphic evolution (e.g., Goffé and Velde, 1984; Franceschelli et al., 1986; Ernst,  
70 1988; Gutiérrez-Alonso and Nieto, 1996; Frey and Robinson, 1999; Bousquet et al., 2008;  
71 Lanari et al., 2012). In this regard, the various results derived from the application of diverse  
72 geothermometric and/or geobarometric methods may also allow the identification and  
73 characterization of superposed tectonometamorphic events, thus improving the knowledge  
74 of the P-T paths and their tectonic significance (e.g., Brown, 1993; Crouzet et al., 2007; Ali,  
75 2010; Lanari et al., 2012; Airaghi et al., 2017).

76 The metamorphism of the Iberian Variscides has been mostly studied on intensely  
77 metamorphosed rocks in order to characterize high-grade events and obtain the P-T-t paths  
78 of suture-related units (e.g., Gil Ibarra et al., 1990; Abalos et al., 1991; Escuder Viruete et  
79 al., 1994; Barbero, 1995; Arenas et al., 1997; Fonseca et al., 1999; López-Carmona et al., 2013;  
80 Martínez Catalán et al., 2014). The low- to very low-grade units have been also studied (e.g.,  
81 Martínez Catalán, 1985; Bastida et al., 1986, 2002; López Munguira et al., 1991; Gutiérrez-  
82 Alonso and Nieto, 1996; Abad et al., 2001, 2002, 2003a; Martínez Poyatos et al., 2001; Nieto  
83 et al., 2005; Vázquez et al., 2007), despite the scarcity of appropriate robust methodologies  
84 to apply in these kind of rocks. Obtaining new results from the low-grade rocks of the Pulo  
85 do Lobo belt, a suture-related low-grade unit in SW Iberia, is of capital importance in order  
86 to understand its significance and tectonometamorphic evolution, that have been cause of  
87 discrepancies, and to reconstruct the overall history of the SW Iberian Variscides.

88 In this work, three different methodologies are applied to a number of samples of the Pulo  
89 do Lobo belt (Fig. 1): (i) X-Ray Diffraction (XRD) in order to identify minerals not easily  
90 recognizable with optical microscopy (fine-grained muscovite, paragonite, mixed-layer  
91 phyllosilicates, etc.) and obtain thermobarometric information via the measurement of  
92 crystallographic parameters (illite “crystallinity” and *b*-cell dimension); (ii) Compositional  
93 maps derived from electron probe microanalysis (EPMA), which enable the recognition of  
94 different tectonometamorphic events by combining mineral composition and microtextural  
95 features (e.g., Airaghi et al., 2017), as well as the application of geothermobarometers based  
96 on chlorite and K-white mica compositions; and (iii) Raman spectroscopy of carbonaceous  
97 material (RSCM) to estimate peak temperatures thanks to an adapted thermometric  
98 calibration. Firstly, the results obtained enables discussing the tectonometamorphic  
99 evolution of the Pulo do Belt. Moreover, the comparison of the different approaches allows  
100 know further their reliability and sensitivity to characterize different geological processes.

101

## 102 2. Geological setting

103 The SW Iberian Variscides resulted from the Devonian-Carboniferous left-lateral oblique  
104 collision of three different terranes: the Central Iberian Zone (CIZ), the Ossa-Morena Zone  
105 (OMZ) and the South Portuguese Zone (SPZ) (Fig. 1a). The boundaries between these  
106 terranes are considered as orogenic sutures (Pérez-Cáceres et al., 2016, and references  
107 therein). Besides the dominant left-lateral shortening kinematics, SW Iberia also attests



108 Mississippian synorogenic sedimentary basins, widespread mafic magmatism and high-  
109 temperature metamorphic areas, which altogether reveal an intraorogenic transtensional  
110 stage (Simancas et al., 2003, 2006; Pereira et al., 2012; Azor et al., 2019).

111 The OMZ is commonly interpreted as a continental piece that drifted from the CIZ (i.e.,  
112 north Gondwana) in early Paleozoic times (Matte, 2001). The OMZ/CIZ suture (Badajoz-  
113 Córdoba Shear Zone) includes early Paleozoic amphibolites with oceanic affinity, eclogite  
114 relicts and intense high- to low-grade left-lateral shear imprint (Burg et al., 1981; Abalos et  
115 al., 1991; Azor et al., 1994; Ordóñez-Casado, 1998; López Sánchez-Vizcaíno et al., 2003;  
116 Pereira et al., 2010). Ediacaran to Carboniferous sedimentary successions with an  
117 unconformity at the base or the Lower Carboniferous characterize the OMZ. Low-grade  
118 regional metamorphism dominates the OMZ, though there are areas of high-temperature /  
119 low-pressure metamorphism associated with Early Carboniferous magmatism (e.g. Bard,  
120 1977; Crespo-Blanc, 1991; Díaz Azpiroz et al., 2006; Pereira et al., 2009).

121 The SPZ is a continental piece considered as a fragment of Avalonia (Pérez-Cáceres et al.,  
122 2017 and references therein). Thus, the OMZ/SPZ boundary is usually interpreted as the  
123 Rheic Ocean suture (Pérez-Cáceres et al., 2015 and references therein). This boundary is  
124 delineated by the Beja-Acebuches Amphibolites (Fig. 1b), a narrow strip of metamafic rocks  
125 that resembles a dismembered ophiolitic succession (from greenschists to metagabbros and  
126 locally ultramafic rocks) (e.g., Bard, 1977; Crespo-Blanc, 1991; Quesada et al., 1994). This  
127 unit was interpreted as a Rheic ophiolite (Munhá et al., 1986; Crespo-Blanc, 1991; Fonseca  
128 and Ribeiro, 1993; Quesada et al., 1994; Castro et al., 1996), though this idea was reconsidered  
129 based on the Mississippian age of the mafic protholits ( $\approx 340$  Ma; Azor et al., 2008). Actually,  
130 the Beja-Acebuches unit is better interpreted as an outstanding evidence of the early  
131 Carboniferous intraorogenic, lithospheric-scale transtensional and magmatic episode that  
132 here obscures the previous suture-related features of the OMZ/SPZ boundary (Pérez-  
133 Cáceres et al., 2015 and references therein). The rocks of the Beja-Acebuches Amphibolites  
134 were affected by a left-lateral ductile shearing occurred at granulite to greenschist facies  
135 conditions, though amphibolite facies conditions were dominant (e.g., Quesada et al., 1994;  
136 Castro et al., 1996; Castro et al., 1999; Díaz Azpiroz et al., 2006). This metamorphism has  
137 been dated at 345-330 Ma (Dallmeyer et al., 1993; Castro et al., 1999), thus suggesting that it  
138 started very shortly after the magmatic emplacement.

139 North of the Beja-Acebuches Amphibolites, the allochthonous Cubito-Moura unit might be  
140 the only witness of the Rheic Ocean suture (Fonseca et al., 1999; Araújo et al., 2005; Pérez-  
141 Cáceres et al., 2015). This unit was emplaced onto the southern OMZ border (Fig. 1b) with  
142 a left-lateral top-to-the-ENE kinematics (Ponce et al., 2012). It contains Ediacaran-Lower  
143 Paleozoic metasediments and Ordovician MORB-featured mafic rocks ( $\approx 480$  Ma; Pedro et  
144 al., 2010) transformed into high-pressure blueschists and eclogites at  $\approx 370$  Ma (Moita et al.,  
145 2005). The high-pressure metamorphism has also been studied by using white mica and  
146 chlorite (and chloritoid pseudomorphs) mineral equilibria (Booth-Rea et al., 2006; Ponce et  
147 al., 2012; Rubio Pascual et al., 2013), yielding peak conditions of 1 GPa at 450 °C.

148 South of the Beja-Acebuches Amphibolites, low- to very low-grade successions crop out in  
149 the SPZ: Devonian siliciclastics, earliest Carboniferous volcano-sedimentary rocks, and a  
150 south-migrating Carboniferous flysch (e.g., Oliveira, 1990). The SPZ can be divided, from





151 north to south, into the Pulo do Lobo belt (see below), the Iberian Pyrite belt (that includes  
152 massive sulphide deposits) and the Carboniferous flysch. The deformation in the SPZ  
153 consists in a south- to southwest-vergent fold and thrust belt with decreasing strain intensity  
154 and age southwards (Oliveira, 1990; Simancas et al., 2004). The metamorphic grade also  
155 decreases southwards, from epizone to diagenesis, through the SPZ (Munhá, 1990; Abad et  
156 al., 2001).

157

## 158 **2.1. Pulo do Lobo belt**

159 The northernmost unit of the SPZ is the Pulo do Lobo belt, whose evolution is intimately  
160 related to the OMZ/SPZ suture (Fig. 1b). The Pulo do Lobo belt constitutes a polydeformed  
161 structure affecting low-grade Devonian-Carboniferous sedimentary formations. These  
162 formations are, from bottom to top (Fig. 1b-c):

163 (i) The Pulo do Lobo formation (s. str.) is constituted by a succession of satiny black to grey  
164 phyllites and fine-grained schists with minor intercalations of quartz sandstones (Fig. 2a).  
165 The presence of abundant segregated quartz veins (pre- to post-folding) is common. The  
166 palynological content suggests a middle Frasnian age (Pereira et al., 2018).

167 (ii) The Ribeira de Limas formation is constituted by phyllites with thin beds of quartz  
168 sandstones and arkoses (Fig. 2b). The presence of palynomorphs also suggests a middle  
169 Frasnian age for this formation (Pereira et al., 2018). The contact with the underlying Pulo  
170 do Lobo formation is gradual, with a progressive increase of sandstones and a decrease of  
171 phyllites upwards. For that reason, we will refer to the Pulo do Lobo and Ribeira de Limas  
172 formations as the lower formations of the Pulo do Lobo belt. Furthermore, these lower  
173 formations share the same structure consisting in three fold-related foliations (Fig. 2a-b;  
174 Pérez-Cáceres et al., 2015). The first foliation of the lower formations ( $S_1$ ) is preserved inside  
175 microlithons of the second foliation ( $S_2$ ); usually, the angle between these two foliations is  
176 high.  $S_2$  is the main foliation and consists in a crenulation-dissolution cleavage that frequently  
177 appears as a millimetric- to centimetric-spaced tectonic banding. This foliation is axial-plane  
178 to north-vergent folds. The third foliation ( $S_3$ ) is a spaced crenulation-dissolution cleavage  
179 that sometimes develops a characteristic decimetric- to metric-scale tectonic banding.  $S_3$  is  
180 associated with upright to slightly south-vergent folds.

181 (iii) The Santa Iría formation is composed by alternating beds of slates and greywackes (Fig.  
182 2c). The greywacke beds show normal grading and erosive base. Paleontological and  
183 palynostratigraphic studies suggest an Upper Famennian age for this formation (Pereira et  
184 al., 2008; 2018). However, an early Carboniferous age is much plausible, since more than  
185 90% of the palynomorphs correspond to reworked material (Lopes et al., 2014) and the  
186 younger detrital zircon population is early Carboniferous (Braid et al., 2011; Pérez-Cáceres  
187 et al., 2017; Pereira et al., 2019). The Santa Iría formation only shows two foliations,  
188 correlative with the last two deformation phases in the lower formations. Therefore, an  
189 unconformity between them is inferred, which also agrees with the age and flysch character  
190 of the Santa Iría formation (Pérez-Cáceres et al., 2015).  $S_2$  is observed as a penetrative slaty  
191 cleavage, while  $S_3$  is a disjunctive crenulation cleavage.



192 According to the evolutionary model proposed by Pérez-Cáceres et al. (2015), the two main  
193 foliations ( $S_2$  and  $S_3$ ) in the Pulo do Lobo belt resulted from the middle/upper Carboniferous  
194 collision between the OMZ and SPZ. On the contrary, the first foliation ( $S_1$ ) in the Pulo do  
195 Lobo belt might have formed during the vanishing stages of Rheic Ocean subduction and/or  
196 the starting Variscan collision, probably at Late Devonian time.

197 The Pulo do Lobo belt contains some decimetric- to metric-scale lenticular bodies of  
198 MORB-featured metamafic rocks intercalated within the phyllites of the Pulo do Lobo  
199 formation and interpreted as a tectonic mélange (the so-called Peramora Mélange; Fig. 1b-c;  
200 Apalategui et al., 1983; Eden, 1991; Dahn et al., 2014). Based on this aspect and on the  
201 supposedly Rheic Ocean derived greenschists, the Pulo do Lobo belt has been classically  
202 interpreted as a pre-collisional subduction-related accretionary prism (Eden and Andrews,  
203 1990; Silva et al., 1990; Eden, 1991; Braid et al., 2010; Ribeiro et al., 2010; Dahn et al., 2014).  
204 However, the recently obtained Mississippian U/Pb zircon ages from the metamafic rocks  
205 (Dahn et al., 2014; Pérez-Cáceres et al., 2015) make difficult to maintain such hypothesis.  
206 More properly, they can be interpreted as mafic intrusions/extrusions in the frame of the  
207 intraorogenic transtensional magmatic event that prevailed in SW Iberia during the  
208 Mississippian. The metamafic rocks display a foliation (equivalent to the  $S_2$  of the enveloping  
209 metasediments) developed at loosely constrained greenschist facies conditions. These rocks  
210 would have been imbricated with the Pulo do Lobo metasediments during the second  
211 deformation phase which caused  $S_2$  (Peramora Olistostrome; Pérez-Cáceres et al., 2015). Our  
212 multidisciplinary metamorphic study of the Pulo do Lobo metasediments provides with  
213 crucial data concerning the tectonic significance of this belt.

214

### 215 3. Samples and analytical methods

216 Eighteen samples were collected from well-exposed outcrops of phyllosilicate-rich detrital  
217 rocks of the Pulo do Lobo belt along two north-south transects perpendicular to the  
218 structural trend. Five samples belong to the Santa Iría formation (unconformable upper  
219 formation) and thirteen to the lower formations (location of samples are in the map and  
220 cross-sections of Fig. 1b-c and the UTM coordinates in supplementary information). As a  
221 whole, the samples were selected in not altered outcrops, far from faults and joints, and were  
222 taken as homogeneous as possible. Sampling design was intended to collect representative  
223 sites, both of the overall stratigraphic succession and along the two transects. We also aimed  
224 to characterize the unconformity between the lower and upper formations from a  
225 metamorphic point of view, since “crystallinity” aspect at first sight seems to be lower in the  
226 Santa Iría formation. Some samples from the lowermost Pulo do Lobo formation were  
227 collected not far from the metabasite lenses of the Peramora Mélange.

228 Samples were examined under the optical microscope and SEM for overall mineralogy,  
229 deformation and minerals/foliations relationships using an environmental scanning electron  
230 microscope FEI model Quanta 400, operating at 15–20 keV (Centro de Instrumentación  
231 Científica-CIC, University of Granada, Spain).

232

233



### 234 3.1. X-Ray diffraction

235 Sample preparation and analysis by XRD were done in the laboratories of the Department  
236 of Mineralogy and Petrology of the University of Granada (Spain). After washing and  
237 cleaning of patinas and oxides, samples were crushed to a <2 mm fraction. The <2  $\mu\text{m}$   
238 fractions were separated by repeated extraction of supernatant liquid after centrifugation,  
239 according to the Stokes' law. Oriented aggregates were prepared by sedimentation on glass  
240 slides of whole-rock and <2  $\mu\text{m}$  fractions (the latter aims to minimize the content of detrital  
241 micas non-re-equilibrated during very low-grade metamorphism, which are generally larger  
242 than 2  $\mu\text{m}$ ; Moore and Reynolds, 1997). Samples were also treated with ethylene glycol  
243 (EGC) to identify illite/smectite or chlorite/smectite mixed-layers on the basis of their  
244 expansibility. Samples were analyzed using a PANalytical X'Pert Pro powder diffractometer  
245 equipped with an X'Celerator detector, CuK $\alpha$  radiation, operated at 45 kV and 40mA, Ni  
246 filter and 0.25° divergence slit. The resulting diffraction diagrams were examined to extract  
247 information on mineralogy based on their characteristic reflections and white mica crystal  
248 data.

249 The Illite “Crystallinity” index (Kübler Index; KI; Kübler, 1968) has been estimated from  
250 the measurement of the full peak-width of K-white mica at half maximum intensity (FWHM  
251 values), expressed as  $\Delta^{\circ}2\theta$  of the Bragg angle. Preparation of samples and experimental  
252 conditions were carried out according to IGCP 294 IC Working Group recommendations  
253 (Kisch, 1991). A step increment of 0.008° 2 $\theta$  and a counting time of 52 s/step were used in  
254 the diffractometer. The KI has been measured in all samples for both the 5 and 10 Å  
255 reflection peaks of K-white mica in order to identify possible effects of other overlapping  
256 phases (Nieto and Sánchez-Navas, 1994; Battaglia et al., 2004). Some XRD traces showing  
257 complex mixture of mixed-layered minerals were decomposed with the MacDiff software  
258 (Petschick, 2004). The FWHM values obtained in the laboratory (x) have been transformed  
259 to Crystallinity Index Standard (CIS) values (y) using the equation  $y=0.972x + 0.1096$  ( $R^2 =$   
260 0.942), obtained from the measure in our lab of the international standards of Warr and Rice  
261 (1994). Finally, they have been expressed in term of traditional KI values using the equation  
262 of Warr and Ferreiro Mähnlmann (2015; ‘CIS’ = 1.1523\*Kübler index ‘Basel lab’ + 0.036).  
263 The lower and upper boundaries of the anchizone in the KI scale are 0.42 and 0.25 °2 $\theta$ ,  
264 respectively (Warr and Ferreiro Mähnlmann, 2015). The thermal range for the anchizone is  
265 estimated in c. 200-300 °C, though the KI cannot be considered as a true geothermometer  
266 (Frey, 1987; Kisch, 1987).

267 The *b*-cell parameter of white mica was obtained from the (060) reflection peak measured  
268 with quartz as internal standard on polished rock-slices cut normal to the sample main  
269 foliation (Sassi and Scolari, 1974). The *b*-cell dimension of K-white mica is often proportional  
270 to the magnitude of phengitic substitution and therefore considered as a proxy of the  
271 pressure conditions during its crystallization. Thus, Guidotti and Sassi (1986) have shown  
272 that *b* values lower than 9.000 Å are typical of low-pressure facies conditions, while *b* values  
273 higher than 9.040 Å are related to rather high-pressure facies metamorphism. Precise  
274 measurements of the basal spacing of white mica ( $d_{001}$ ) have also been made, using quartz  
275 from the sample itself as internal standard.  $d_{001}$  is related to the paragonitic Na/K substitution



276 (Guidotti et al., 1992), thereby approximately reflecting the temperature of formation  
277 (Guidotti et al., 1994).

278

### 279 3.2. EPMA-derived X-Ray compositional maps and chlorite thermometry

280 From all of the collected samples, we selected those with the larger phyllosilicate grain-size  
281 for electron probe microanalysis (EPMA). Thus, three carbon-coated polished thin-sections  
282 were studied. The selected samples (PLB-84, PLB-88 and PLB-93) belong to the lower  
283 formations of the Pulo do Lobo belt (Fig. 2d-e). The Santa Iría samples could not be studied  
284 due to the tiny grain size of the slaty minerals (commonly less than 3  $\mu\text{m}$ ).

285 Compositional maps and accurate spot analyses were performed on a JEOL JXA-8230  
286 EPMA at the Institut des Sciences de la Terre (ISTerre) in Grenoble (France), according to  
287 the analytical procedure proposed by de Andrade et al. (2006) and Lanari et al. (2014a). The  
288 data acquisition was made in wavelength dispersive spectrometry mode (WDS). Ten  
289 elements (Si, Ca, Al, K, Mn, Na, P, Ti, Fe and Mg) were analyzed using five WD  
290 spectrometers: TAP crystal for Si and Al, PETL for Ti and P, TAPH for Na and Mg, PETH  
291 for K and Ca, and LIFH for Mn and Fe. The standardization was made by using certified  
292 natural minerals and synthetic oxides: Wollastonite (Si, Ca), Corundum (Al), Orthoclase (K),  
293 Rhodonite (Mn), Albite (Na), Apatite (P), Rutile (Ti), Hematite (Fe), and Periclase (Mg). X-  
294 Ray maps were obtained by adding successive adjacent profiles. Beam current of 100 nA and  
295 beam size spot (focused) were used. The step (pixel) size was 1  $\mu\text{m}$  and dwell time was 200-  
296 300 msec per pixel. Spot analyses were obtained along the profiles within the mapping at 15  
297 kV accelerating voltage, 12 nA beam current and 2  $\mu\text{m}$  beam size spot (focused). The on-  
298 peak counting time was 30 sec for each element and 30 sec for two background  
299 measurements at both sides of the peak. ZAF correction procedure was applied. The internal  
300 standards were orthoclase and/or chromium-augite (Jarosewich et al., 1980), which were run  
301 (3 points on each standard) after each profile in order to monitor instrumental drift and  
302 estimate analytical accuracy. Drift correction was made, if necessary, using the corresponding  
303 regression equation.

304 The WDS X-Ray maps were then processed with XMapTools  
305 (<http://www.xmaptools.com>), a MATLAB©-based graphical user interface program to  
306 process the chemical maps, link them to thermobarometric models and estimate the  
307 pressure-temperature conditions of crystallization of minerals in metamorphic rocks (Lanari  
308 et al., 2014a). The compositional maps were standardized with the spot analyses measured  
309 along the profiles and mineral compositions were plotted into binary and ternary diagrams  
310 using the interface modules *Chem2D* and *Triplot3D*. Chemical maps of amount of tetrahedral  
311 aluminum ( $\text{Al}^{\text{IV}}$ ) of chlorites were acquired, because is at the base of many empirical chlorite  
312 thermometers (e.g. Cathelineau and Nieva, 1985; Cathelineau, 1988). The temperature  
313 conditions were estimated for each chlorite pixel of the maps using the chlorite thermometer  
314 of Lanari et al. (2014b), as well as the approaches of Vidal et al. (2006) and Bourdelle et al.  
315 (2013), which are summarized in the supplementary information.

316 In addition to the above mentioned compositional maps, white micas from seven carbon-  
317 coated thin sections of the lower formations of the Pulo do Lobo belt were analyzed before



318 with a Jeol four-spectrometer microprobe (JXA-8200 Superprobe) at the University of  
319 Huelva (Spain). A combination of silicates and oxides were used for calibration. Single point  
320 analyses were obtained with 10 nA probe current, 1-5  $\mu\text{m}$  spot size, and 20 kV of acceleration  
321 voltage.

322

### 323 3.3. Raman Spectroscopy of carbonaceous material

324 Beyssac et al. (2002a) calibrated a technique for the quantification of peak metamorphic  
325 temperature, which can be used even in the absence of specific mineral assemblages  
326 necessary for classical thermobarometric estimates. This technique, Raman Spectroscopy of  
327 Carbonaceous Material (RSCM), is based on the observation that sedimentary carbonaceous  
328 material is progressively transformed into graphite at increasing temperature. Beyssac et al.  
329 (2002a) found a linear relationship between temperature and the structural state of CM  
330 quantified by Raman microspectroscopy. Because of the irreversible character of  
331 graphitization, CM structure is not sensitive to the retrograde path during exhumation of  
332 rocks, but only depends on the maximum temperature reached during metamorphism  
333 (Beyssac et al., 2002a). Temperature can be determined in the range 330-650°C with a  
334 calibration-attached accuracy of  $\pm 50$  °C due to uncertainties on petrologic data used for the  
335 calibration. Relative uncertainties on temperature are, however, much smaller (around 10-15  
336 °C; Beyssac et al., 2004). For temperature below 330 °C, Lahfid et al. (2010) performed a  
337 systematic study of the evolution of the Raman spectrum of CM in low-grade metamorphic  
338 rocks in the Glarus Alps (Switzerland). They showed that the Raman spectrum of CM is  
339 slightly different from the spectrum observed at higher temperature and they established a  
340 quantitative correlation between the degree of ordering of CM and temperature.

341 In this work, twelve representative thin-sections previously examined by optical microscopy  
342 were selected. From them, ten samples were finally analyzed: eight samples belong to the  
343 lower formations (Pulo do Lobo and Ribeira de Limas formations), while the other two  
344 belong to the Santa Iría formation. Polished thin-sections cut perpendicularly to the foliation  
345 were analyzed at the Institut de Minéralogie, de Physique des Matériaux et de Cosmochimie  
346 at the Sorbonne University of Paris (France). We followed closely the analytical procedure  
347 described by Beyssac et al. (2002a, b; 2003; see supplementary information). More than 15  
348 Raman spectra (Fig. 3) were obtained for each sample using a Renishaw InVIA Reflex  
349 microspectrometer equipped with a 514.5 nm Modulaser argon laser under circular  
350 polarization. The laser was focused by a DMLM Leica microscope, and laser power was set  
351 below 1 mW at the sample surface. The Rayleigh diffusion was eliminated by edge filters and  
352 the signal was dispersed using a 1800 g/mm grating and finally analyzed by a Peltier cooled  
353 RENCAM CCD detector. The recorded spectral window was large to correctly set the  
354 background correction, from 700 to 2000  $\text{cm}^{-1}$  in case of low-temperature samples. Before  
355 each session, the spectrometer was calibrated with a silicon standard. CM was systematically  
356 analyzed behind a transparent adjacent mineral, generally quartz or white mica grains oriented  
357 along  $S_1$ . For a full description of the temperature calculations see the supplementary  
358 information.

359



## 360 4. Results

361 According to SEM analysis, all the samples correspond to slates or phyllites with  
362 phyllosilicates smaller than 500  $\mu\text{m}$ , composed of variable quartz + K-white mica  $\pm$  chlorite  
363  $\pm$  feldspar  $\pm$  ore and accessory minerals (Fig. 2d-f). Samples from the Santa Iría formation  
364 have much smaller grain-size and apparently lower “crystallinity” (Fig. 2f). The first foliation  
365  $S_1$  is defined by the largest micas and chlorites (Fig. 2d-e), being folded by microscopic- to  
366 centimetric-scale tight folds of the second deformation phase (Fig. 2a-b, d-e). The second  
367 foliation  $S_2$  is the main foliation at outcrop (Fig. 2a-c), but the development of phyllosilicates  
368 (mostly white mica) is lesser than  $S_2$ . The third foliation  $S_3$  is much less penetrative (Fig. 2a-  
369 c) and does not develop phyllosilicates. Large detrital phyllosilicate clasts have not been  
370 observed.

371

### 372 4.1. X-Ray diffraction

373 The mineralogy and crystal parameters obtained from the 18 samples of the Pulo do Lobo  
374 belt are summarized in Table 1. The results of KI values, b-cell parameter and  $d_{001}$  analyzed  
375 in K-white mica, obtained from whole-rock and  $<2 \mu\text{m}$  fractions are very similar, which  
376 suggests that detrital micas re-equilibrated during metamorphism.

377 The mineralogy of the samples is relatively simple:  $Qz + Ms + Fsp + Chl \pm Pg \pm C/S$ . The  
378 slates of the Santa Iría formation have quartz, muscovite and chlorite, with chlorite/smectite  
379 interlayers (C/S) in some samples. In the lower formations, besides quartz and muscovite,  
380 chlorite is present in almost all of the samples, paragonite appears in most of them, and  
381 chlorite/smectite interlayers are occasional.

382 KI values measured in the 10  $\text{\AA}$  peak of white mica from the  $<2 \mu\text{m}$  fraction are shown in  
383 Table 1 and Fig. 1c with a relative colour bar from orange (lower values) to green (higher  
384 values). Values of the Santa Iría samples ( $n=5$ ) range from 0.20 to 0.26  $\Delta^\circ 2\theta$ , the mean value  
385 being 0.23 (standard deviation 0.02). As for the lower formations ( $n=12$ ), KI values range  
386 from 0.17 to 0.22, the mean value being 0.19 (standard deviation 0.02). KI values measured  
387 in the 5  $\text{\AA}$  peak (not shown) are very similar to those of the 10  $\text{\AA}$  peak.

388 The measured b-cell parameter of white mica varies in a close range around 9  $\text{\AA}$  (8.991-9.002).  
389 Mean value is 8.995  $\text{\AA}$  (standard deviation 0.003) for the Santa Iría formation samples, and  
390 8.997  $\text{\AA}$  (standard deviation 0.003) for the samples of the lower formations.  $d_{001}$  values  
391 average 9.992  $\text{\AA}$  (standard deviation 0.004) and differ slightly between upper and lower  
392 formations, being higher in the upper formation.

393 The results obtained through X-Ray diffraction denote very low- to low-grade metamorphic  
394 conditions due to the presence of C/S and KI values between 0.17-0.26  $\Delta^\circ 2\theta$ . In addition,  
395 b-cell parameters show a low-pressure metamorphic gradient.

396

### 397 4.2. Compositional maps and chlorite thermometry

398 X-Ray maps show the distribution of major elements and allow identifying white mica,  
399 chlorite, and some albite porphyroblasts, with ilmenite and rutile as accessory minerals (Fig.





400 4a-b). Although quartz is abundant in all of the samples, the zoomed selected areas for X-  
401 ray mapping (composed mostly by phyllosilicates) do not contain quartz (Fig. 4a-b). White  
402 mica is abundant along both  $S_1$  and  $S_2$  foliations (Fig. 2d-e and 4b). Chlorite is found mostly  
403 along  $S_1$ , being very scarce and small-sized along  $S_2$  (Fig. 2e and 4b), with the exception of  
404 sample PLB-93 where chlorite is similar in amount in both foliation domains (Fig. 4b).

405 Mapped compositions of end-members of white mica and chlorite have been plotted in the  
406 ternary diagrams of Figure 5. The composition of white mica is similar in the three maps. It  
407 is close to muscovite, with 25% of pyrophyllite and very scarce celadonite content (Fig. 5a).  
408 The high content of pyrophyllite (high amount of interlayer vacancies) is typical of low-  
409 pressure illite compositions. Figure 6 shows white mica compositional ratios, which can be  
410 related to P/T conditions: they present low degree of Na substitution and low phengitic  
411 component, thus being close to the muscovite end-member. These results point to low-  
412 pressure conditions and agree well with XRD results: low  $b$ -cell parameter and high  $d_{001}$   
413 (Table 1).

414 Chlorite compositions are variable, though all of them have in common  $\approx 50\%$  clinocllore  
415 + daphnite and  $\approx 50\%$  amesite + sudoite (Fig. 5b). Chlorites in sample PLB-88 are poor in  
416 amesite with a large variation of clinocllore + daphnite and sudoite. In sample PLB-84  
417 chlorites, variable compositions between amesite and sudoite indicate a variation of  $Al^{IV}$ ,  
418 which implies an increase of temperature from rims to cores as shown in the chemical maps  
419 of Fig. 4c. Finally, PLB-93 chlorites are poor in sudoite, thus suggesting higher average  
420 temperatures. Altogether, chlorite compositional data suggest the presence of two end-  
421 members: sudoite-rich low-temperature (PLB-88), and amesite-rich high-temperature (PLB-  
422 93).

423 Maps of  $Al^{IV}$  in chlorites have been represented in Fig. 4c. Sample PLB-88 shows lower  $Al^{IV}$   
424 content ( $\approx 1.1$ - $1.3$  apfu) than sample PLB-93 ( $\approx 1.3$ - $1.5$  apfu). In sample PLB-84, some large  
425 chlorite grains oriented along  $S_1$  are zoned, with higher  $Al^{IV}$  content in the cores ( $\approx 1.4$  apfu)  
426 than in the rims ( $\approx 1.0$  apfu; see white square in Fig. 4c). According to the empirical  
427 calibration of Cathelineau (1988),  $Al^{IV}$  in chlorites increases with temperature. Thus, the  $Al^{IV}$   
428 content in chlorites manifests different temperatures in different samples, and also from core  
429 to rim in singular grains.

430 Temperature maps have been obtained with the semi-empirical thermometer of Lanari et al.  
431 (2014b), assuming that  $Fe^{2+}$  is the Fe total (Fig. 4d). Temperatures range between 100-200  
432 °C in sample PLB-88, 150-350 °C in sample PLB-84, and 200-450 °C in sample PLB-93.  
433 Tiny chlorites developed along  $S_2$  show lower temperatures than larger and more abundant  
434 chlorites along  $S_1$ , with the exception of sample PLB-93. Furthermore, some large chlorites  
435 oriented along  $S_1$  are zoned, showing high-temperature relic cores (350-450 °C; see white  
436 insets in Fig. 4c-d) surrounded by low-temperature rims (150-250 °C).

437 To test Vidal et al. (2005, 2006) and Bourdelle et al. (2013) approaches, an area of  
438 representative chlorites in an  $S_1$  microlithon was selected from each map (see red insets in  
439 Fig. 4d). Corresponding chlorite compositions were extracted and introduced in the chlorite-  
440 quartz-water equilibria (Fig. 7a, Vidal et al., 2005, 2006; Fig. 7b, Bourdelle et al., 2013). The  
441 temperature estimates (Fig. 7) are fairly similar with both methods, averaging 120-230 °C in  
442 sample PLB-88 and 150-380 °C in sample PLB-84. This is also in agreement with the





443 temperature maps calculated with the Lanari et al. (2014a) model. Only the sample PLB-93  
444 shows a divergence on temperature averages: mostly 200-250 °C with the thermometer of  
445 Bourdelle et al. (2013), and 250-350 °C with the one of Vidal et al. (2005, 2006). Nevertheless,  
446 the Bourdelle thermometer predicts temperatures up to 380-400°C. In both cases, the higher  
447 temperature analyses are obtained from crystal cores and belong to the sample PLB-93.

448

### 449 4.3. RSCM thermometry

450 The ratio parameters and corresponding maximum temperatures obtained from all the  
451 spectra analyzed are shown in the supplementary information. The Raman spectra were  
452 decomposed into bands following the appropriate fitting procedure described in Beyssac et  
453 al. (2002a) for the lower formations (high-temperature Raman spectra; ratio parameter R2)  
454 and Lahfid et al. (2010) for the Santa Iría formation (low-temperature Raman spectra; ratio  
455 parameters RA1 and RA2). The average temperatures are shown in Table 1 and Fig. 1c with  
456 a relative colour bar from red (higher temperature) to blue (lower temperature). The average  
457 temperatures for the lower formations range from 420 to 530 °C, with a mean value of 468  
458 °C (standard deviation of 35). The highest temperatures are found in samples PLB-82 (530  
459 °C) and PLB-93 (495 °C), while the remaining ones do not exceed 480 °C. As for the Santa  
460 Iría formation, temperatures are lower (315-330 °C; Table 1) than in the underlying  
461 formations.

462

## 463 5. Interpretation and discussion

### 464 5.1. Deformation/metamorphism relationships

465 The obtained analytical results must be interpreted in the context of the Variscan evolution  
466 of the Pulo do Lobo belt. As described above, two regional deformational events D<sub>1</sub> and D<sub>2</sub>  
467 gave way to the development of foliations (Devonian S<sub>1</sub> and Carboniferous S<sub>2</sub>) accompanied  
468 by metamorphic phyllosilicate growth (M<sub>1</sub> and M<sub>2</sub>). In the cross-sections of Fig. 1c, KI values  
469 derived from XRD and average temperature from RSCM are represented. The lowest  
470 metamorphic grade (green and blue colours) corresponds to the Santa Iría formation.  
471 Moreover, Table 2 summarizes the relationship between deformation and metamorphism of  
472 the Pulo do Lobo belt in the context of the Variscan tectonic evolution of SW Iberia (Pérez-  
473 Cáceres et al., 2015).

474 The textural observations evidence that in most samples of the lower formations M<sub>1</sub> was the  
475 main crystallization event, developing abundant and large-sized white mica and chlorite in S<sub>1</sub>  
476 microlithons, while M<sub>2</sub> gave way to small-sized white mica (e.g., Fig. 2e and map 1 in Fig. 4).  
477 On the other hand, polydeformed rocks commonly show previously grown minerals rotated  
478 towards a new foliation developed at lower-grade conditions, without new crystallization.  
479 This can be the case of the white micas that define S<sub>2</sub> in some samples (illustrated in Fig. 2d),  
480 which, in turn, is not contradictory with the similar chemical composition of S<sub>1</sub> and S<sub>2</sub> micas  
481 (Fig. 5a). As shown in our samples, S<sub>1</sub> is variably crenulated by D<sub>2</sub>, so that M<sub>1</sub> minerals are  
482 variably rotated towards S<sub>2</sub>. Consequently, the metamorphic data obtained from the samples  
483 of the lower formations will be ascribed to D<sub>1</sub>-M<sub>1</sub>. Sample PLB-93 might represent an  
484 exception, since its slightly higher RSCM and chlorite-derived temperatures might be due to



485 nearby intrusions (Fig. 1b and 1c.1). At this respect, it is important to note the Mississippian  
486 transtensional event (basins development and abundant mafic magmatism) that took place  
487 between  $D_1$  and  $D_2$  (Pérez-Cáceres et al., 2015). The characterization of  $M_2$  can be done by  
488 studying the samples from the Santa Iría formation, which are only affected by  $S_2$   
489 accompanied by small-sized phyllosilicate growth (Fig. 2f).

490

## 491 5.2. First tectonothermal event (Devonian $M_1$ )

492 The observed mineral association ( $Qz + Ab + Ms + Chl \pm Pg$ ), together with the presence  
493 of C/S is compatible with low-grade metamorphic conditions (Table 1). White mica  
494 “crystallinity” values ( $0.17-0.22 \Delta^{\circ}2\theta$ ; average 0.19) are always in the range of the epizone  
495 (low-grade or greenschists facies;  $>300$  °C; Frey, 1987; Kisch, 1987, Warr and Ferreiro  
496 Mähnlmann, 2015), in accordance with the values reported by Abad et al. (2001) in a more  
497 general study of the diagenetic-metamorphic evolution of the South Portuguese Zone  
498 metapelites. Nevertheless, both the values of KI, still far from  $0.14 \Delta^{\circ}2\theta$ , and their variability,  
499 suggest that temperature was not high enough as to stabilize a highly crystalline white mica  
500 at high epizone conditions (Abad et al., 2006). This is in agreement with the low Na content  
501 of K-micas coexisting with paragonite (Fig. 6), meaning a very-low temperature position in  
502 the muscovite-paragonite solvus for natural quasi-binary Pg-Ms pairs (Guidotti et al., 1994).  
503 By contrast, the maximum temperatures obtained with RSCM geothermometry are  
504 surprisingly high (420-530 °C; average 470 °C; corresponding to very high epizone or even  
505 medium-grade conditions; Table 1).

506 The composition of paired chlorite and white mica is normally used to calculate pressure and  
507 temperature (e.g., Vidal et al., 2006), but multi-equilibrium approach was not successful  
508 because the P-T equilibrium conditions did not converge. This result is indicative of chemical  
509 disequilibrium, precluding their use as a reliable geothermobarometer in this case. The  
510 temperatures calculated from chlorite compositions following various approaches (Vidal et  
511 al., 2006, Fig. 7a; Bourdelle et al., 2013, Fig. 7b; Lanari et al., 2014a, Fig. 4d) are as follow:  
512 120-230 °C for sample PLB-88, 150-380 °C for sample PLB-84, and 250-400 °C for sample  
513 PLB-93 and a small population of chlorite cores from sample PLB-84 (Figs. 4 and 7, and  
514 Table 1). The slightly higher temperature of sample PLB-93 is inferred from its highest white  
515 mica “crystallinity” ( $0.17 \Delta^{\circ}2\theta$ ), high RSCM temperature (495 °C), high-temperature  
516 (amesite-rich) chlorite and higher chlorite thermometry (Table 1), and can be explained by  
517 its nearness to metric-scale mafic igneous bodies of the Peramora Mélange (located at  $\approx 200$   
518 m to the south; Pérez-Cáceres et al., 2015) and/or to a granite stock (located at  $\approx 5$  km to the  
519 west) (Fig. 1b).

520 In our samples there is some evidence of chlorite retrogression: (i) the chemical  
521 disequilibrium showed by the white mica/chlorite geothermobarometer, (ii) the presence of  
522 C/S mixed layers not stable in the epizone (e.g. Potel et al., 2006), (iii) the difference between  
523 temperature estimates from crystal rims to cores, and the higher temperature relic cores  
524 preserved in large chlorites defining  $S_1$  (Fig. 4c-d), and (iv) the previously reported XRD and  
525 TEM data of chlorite retrograded to smectite and corrensite in the Pulo do Lobo belt (see  
526 fig. 1 in Nieto et al., 2005). The existence of chlorites with different compositions crystallized  
527 at different temperatures is the usual scenario (e.g., Vidal et al., 2006, 2016; Lanari et al., 2012;



528 2014a and b; Grosch et al., 2012; 2014; Cantarero et al., 2014). In such situation, the  
529 definition of a single temperature and pressure attributable to peak conditions is difficult.  
530 The maximum temperature showed by chlorite relic cores is 350-450 °C (Fig. 4d), which is  
531 more in accordance with the conditions estimated for M<sub>1</sub> by means of white mica  
532 “crystallinity” and RSCM data.

533 An issue that deserves some discussion is the difference in temperature estimates between  
534 RSCM and other techniques. RSCM thermometry records the peak temperature and is not  
535 sensitive to the retrograde path. Alternatively, other methods based on phyllosilicate  
536 compositions are prone to record reequilibration during the retrograde path; thus, they rarely  
537 record the peak conditions, except perhaps in the core of certain large crystals. Therefore,  
538 RSCM and phyllosilicate-based methods do not record the same information on  
539 temperature, being in fact complementary. The analyzed CM gains were carefully checked by  
540 microtextural observation and spectral geometry to make sure that these grains are actually  
541 derived from in situ organic matter graphitized during metamorphism.

542 In our case study, at the high peak temperature given by the RSCM thermometry, minerals  
543 such as biotite or garnet are expected to crystallize in metasediments, though they have not  
544 been observed in our samples. The absence of such minerals can be due to whole-rock  
545 composition, and explained by growth inhibition related to Na-excess, as evidenced by the  
546 presence of albite and paragonite in our samples. Another possible explanation could be the  
547 higher sensitivity of CM graphitization to fast reequilibration during a short-time thermal  
548 event. Thus, the Mississippian intrusions subsequent to M<sub>1</sub> in the Pulo do Lobo formation  
549 (see description in section 2) could have exerted a fast and locally intense thermal imprint  
550 that influenced CM but not the crystal chemistry of silicates. Moreover, recrystallization  
551 processes are not only function of temperature, but also promoted by deformation/stress,  
552 time, fluid/rock ratio (Merriman and Frey, 1999). Observations of this kind (differing  
553 reaction kinetics between organic and inorganic material (e.g. illite) in a contact metamorphic  
554 setting can be found in Olsson (1999) and Abad et al. (2014). Regarding the time of geological  
555 processes, Mori et al. (2017) investigated the importance of heating duration for RSCM  
556 thermometry by studying graphitization around dykes. They showed that small-scale  
557 intrusions generating short thermal events modify the structure of CM in the surrounding  
558 rocks, to conclude that CM crystallinity is clearly related to contact metamorphism. The  
559 influence of low-pressure contact aureoles on RSCM temperature patterns is further  
560 supported by the results obtained by Hilchie and Jamieson (2014), who concluded that the  
561 variation of RSCM temperatures can be controlled by the subsurface geometry of a pluton.  
562 Finally, the long-distance thermal influence of plutonic intrusions on low-grade rocks located  
563 as far as 10 km has already been evidenced (e.g., Merriman and Frey, 1999; Martínez Poyatos  
564 et al., 2001) and could also be recorded by RSCM thermometry in our samples.

565

### 566 5.3. Second tectonothermal event (middle/upper Carboniferous M<sub>2</sub>)

567 The mineralogy of the Santa Iria samples (Qz + Ms + Chl ± C/S) is compatible with very  
568 low- to low-grade conditions. The K-white mica “crystallinity” values (0.20-0.26 Δ°2θ;  
569 average 0.23) point to lower epizone conditions, very close to the boundary with the



570 anchizone ( $\approx 300$  °C; Frey, 1987; Kisch, 1987). The temperatures calculated by RSCM in two  
571 samples (315 and 330 °C) are compatible with the KI data of XRD analysis.

572 Our metamorphic data corroborate the existence of an unconformity between the lower and  
573 upper formations of the Pulo do Lobo belt (Pérez-Cáceres et al., 2015). The lower formations  
574 record a Devonian tectonothermal event that reached epizone or lower greenschist facies  
575 conditions ( $M_1$  with generalized phyllosilicate growth at temperatures as high as 450 °C),  
576 while the overlying upper formation records a middle/upper Carboniferous tectonothermal  
577 event close to the anchizone/epizone boundary ( $M_2$  with small-sized phyllosilicate growth at  
578 temperatures  $\approx 300$ -330 °C; Table 1). Obviously,  $M_2$  also affected somehow the lower  
579 formations, being, at least in part, the responsible for the observed retrogression of  $M_1$   
580 chlorite and/or crystallization of new chlorites at lower temperature.

581

#### 582 **5.4. Pressure conditions**

583 The measured *b*-cell parameters of K-white mica (in a short range between 8.991-9.002 Å;  
584 average 8.996; standard deviation 0.003) are very similar in the lower and upper formations  
585 of the Pulo do Lobo belt. Thus, the *b* parameter is consistently homogeneous and reflects  
586 very low phengite substitution in mica, as expected at low-pressure settings (Potel et al., 2006,  
587 2016), near the intermediate pressure gradient boundary (Guidotti and Sassi, 1986).

588 In agreement with the low *b*-cell parameters, the composition of K-white mica is close to  
589 muscovite with very low celadonite and higher pyrophyllite content (Fig. 5a), as expected for  
590 illite-rich mica formed at low-pressure gradients. In the case of high- or medium-pressure  
591 conditions, a continuous trend in mica compositions would be found reflecting the  
592 decompression path after the peak pressure, while the *b*-cell parameter would represent an  
593 average value of the range of mica compositions found in the sample (Abad et al., 2003b).  
594 On the contrary, at low-pressure settings, the overall range of recorded pressure is very short  
595 and micas present similar compositions and *b*-cell parameters among the various samples, as  
596 in the case of the Pulo do Lobo samples (Figs. 5a and 6, and Table 1).

597 The Pulo do Lobo belt has been classically interpreted as a pre-collisional subduction-related  
598 accretionary prism, based on the MORB geochemistry of their mafic rocks (see section 2.1).  
599 According to this classical interpretation, features typical of modern subduction systems  
600 should be expected, such as high-pressure metamorphic gradient remnants of partial  
601 subduction/exhumation in an accretionary wedge (e.g., Platt, 1986; Ernst, 2005), or slices of  
602 oceanic slab-derived lithologies (varied mid-ocean ridge metaigneous lithologies and also  
603 deep ocean bottom metasediments). Thus, recent works on the Makran accretionary prism  
604 (Omrani et al., 2017) and the subduction system of Japan (Endo and Wallis, 2017) describe  
605 an accretionary mélange complex composed of pelagic sedimentary rocks, ophiolites,  
606 greenschists, amphibolites, and blueschists with high-pressure minerals such as lawsonite and  
607 glaucophane. On the contrary, most of the geological data concerning the Pulo do Lobo belt  
608 do not back up such interpretation (see section 2.1), and our new results about pressure  
609 conditions are also in disagreement. The only suspect of high-pressure gradient in the Pulo  
610 do Lobo belt is the interpretation of some rhomboidal aggregates of epidote porphyroblasts as  
611 the remnants of supposed lawsonite grown previously to  $S_2$  in some samples of Pulo do



612 Lobo mafic schists (Rubio Pascual et al., 2013). However, no analytical data have been  
613 presented to support the lawsonite pseudomorphs.

614

## 615 **6. Conclusions**

616 Eighteen samples of metapelites from the Pulo do Lobo belt have been studied to  
617 characterize their Variscan low-grade metamorphism. The microstructural analysis of the  
618 samples of the lower formations (Devonian Pulo do Lobo and Ribeira de Limas) shows the  
619 existence of two superposed low-grade tectonothermal events with associated foliation and  
620 phyllosilicate growth (S<sub>1</sub>-M<sub>1</sub> and S<sub>2</sub>-M<sub>2</sub>; Table 2). M<sub>2</sub> was less intense, being the only event  
621 that affected the overlying Carboniferous Santa Iria formation. The regional geology also  
622 shows that a Mississippian thermal (magmatic-derived) event occurred in-between M<sub>1</sub> and  
623 M<sub>2</sub>.

624 M<sub>1</sub> and M<sub>2</sub> correspond to the chlorite zone, but M<sub>1</sub> entered the epizone (greenschists facies  
625 with temperatures up to ≈450 °C), while M<sub>2</sub> did not exceed the anchizone-epizone boundary  
626 (≈300 °C).

627 The temperatures obtained from RSCM are higher compared to the ones derived from  
628 chlorite geothermometry and white mica data. The discrepancy can be explained by the fact  
629 that RSCM records the true maximum temperature, being not affected by retrogression as  
630 other methods do. In addition, this difference can be the consequence of the high sensitivity  
631 of CM to quickly equilibrate at maximum temperatures during short thermal events due to  
632 magmatic intrusions emplaced during the Mississippian thermal event.

633 Thermodynamic disequilibrium between white mica and chlorite has precluded their use for  
634 geothermobarometry, and a variety of data (including the existence of relic high-temperature  
635 chlorite cores, the presence of chlorite/smectite mixed layers, or the very-low temperatures  
636 calculated with chlorite geothermometers) indicate chlorite retrogression after M<sub>1</sub>  
637 metamorphic climax and crystallization of new chlorite grains at lower temperature.

638 The low-pressure conditions derived from white mica indicators (very low celadonite content  
639 and *b*-cell values) are incompatible with the high-pressure metamorphic gradient expected in  
640 a subduction-related accretionary wedge, which has been the classical interpretation of the  
641 Pulo do Lobo belt.

642

643

## 644 **Acknowledgements**

645 This work was supported by the projects CGL2011-24101 (Spanish Ministry of Science and  
646 Innovation), CGL2015-71692-P and CGL2016-75679-P (Spanish Ministry of Economy and  
647 Competitiveness), RNM-148 and RNM-179 (Andalusian Government) and BES-2012-  
648 055754 (Doctoral scholarship to I. Pérez-Cáceres from the Spanish Ministry of Science and  
649 Innovation). The Raman facility in Paris has been funded by the City of Paris (Emergence  
650 program). We thank Valérie Magnin for her assistance with the microprobe analysis in  
651 Grenoble and Pierre Lanari for his support with thermodynamic software.



## 652 Figure captions

653 **Figure 1.** a) Location of the studied area in the SW of the Iberian Massif (in grey). CIZ: Central  
654 Iberian Zone, OMZ: Ossa-Morena Zone, SPZ: South Portuguese Zone. b) Geological map of the  
655 Pulo do Lobo belt and other units related to the OMZ/SPZ boundary with indications of the two  
656 cross-sections studied. c.1-2) Geological cross-sections of the Pulo do Lobo belt (see b for location)  
657 (modified from Martínez Poza et al., 2012 and Pérez-Cáceres et al., 2015). Numbered red circles in  
658 b-c locate the samples studied. Big circles show the KI values for 10 Å reflection peaks of K-white  
659 mica and the average RSCM temperatures, with the relative colour bar according to the results shown  
660 in Table 1. BAA: Beja-Acebuches Amphibolites, M: metabasalts, PL: Pulo do Lobo formation, RL:  
661 Ribeira de Limas formation, SI: Santa Iría formation.

662 **Figure 2.** Pictures of the Pulo do Lobo rocks illustrating deformation at outcrop scale: a) Pulo do  
663 Lobo formation, b) Ribeira de Limas formation, c) Santa Iría formation. Microphotographs from  
664 thin-sections: d) Cross-polarized light image of sample PLB-84 (Pulo do Lobo formation), e) SEM-  
665 BSE image of sample PLB-88 (Ribeira de Limas formation), f) Cross-polarized light images of sample  
666 PLB-71 (Santa Iría formation).

667 **Figure 3.** Representative Raman spectra of CM across the Pulo do Lobo belt from low temperature  
668 (bottom; Santa Iría formation) to high temperature (top; lower formations) including the average  
669 maximum temperatures (°C) for each sample. Vertical scale for spectrum intensity is arbitrary. See  
670 Fig. 1 for sample location and Table 1 and supplementary information for RSCM data.

671 **Figure 4.** X-Ray maps of the three selected samples analyzed by EPMA and processed with  
672 XMapTools. The samples belong to the lower formations of the Pulo do Lobo belt (sample PLB-88:  
673 Ribeira de Limas formation; samples PLB-84 and PLB-93: Pulo do Lobo formation; the latter (PLB-  
674 93) is close to Early Carboniferous igneous intrusions). a) EPMA BSE photographs. b) Mineral maps.  
675 c) Al<sup>IV</sup> content map in chlorites, which increases with temperature. The white square highlights the  
676 zonation of a chlorite grain from core to rim. d) Temperature maps of chlorite using the Lanari et al.  
677 (2014a) geothermometer assuming all iron as ferrous. White squares show selected areas illustrating  
678 higher-temperature chlorite cores. Red squares show the selected areas (representative of S<sub>1</sub> foliation)  
679 used for chlorite-quartz-water geothermometric calculations shown in Fig. 7.

680 **Figure 5.** Ternary plots of all the analyzed white micas (a) (Cel: celadonite, Mus: muscovite, Prl:  
681 pyrophyllite) and chlorite (b) (Cli+Daph: clinocllore + daphnite, Am: amesite, Sud: sudoite) plotted  
682 with the XmapTools TriPlot3D module. Colour bars refer to the number of mica/chlorite pixels  
683 analyzed.

684 **Figure 6.** Compositional diagram of white micas showing Na/(Na+K) vs Si/Al (atomic ratios) for 31  
685 EPMA point analyses from seven samples of the lower formations of the Pulo do Lobo belt (different  
686 symbology, for each sample). Point analyses were obtained on the microprobe at the University of  
687 Huelva (Spain). Qualitative information about temperature and pressure conditions are respectively  
688 according to Guidotti et al. (1994), Coggon and Holland (2002), Parra et al. (2002), Massonne and  
689 Schreyer (1987) and Massonne and Szpurka (1997).

690 **Figure 7.** Histograms of temperatures obtained using the chlorite-quartz-water geothermometer of  
691 Vidal et al. (2006) (a) and Bourdelle et al. (2013) (b) on selected representative S<sub>1</sub> chlorites (see red  
692 squares in Fig. 4d for location). *n* represents the number of chlorites that could be used for each  
693 calibration. The number of analyses is lower in those with Vidal et al. (2006) approach because the  
694 assumption that the Si content of chlorite is lower than 3 apfu.

695

696





697 **Table captions**

698 **Table 1.** Samples and results obtained by XRD (<2 μm fraction), white mica and chlorite  
699 compositions, temperature ranges from chlorite thermometry, and average RSCM thermometry. KI  
700 values and average RSCM temperatures show a relative colour-bar scale. Mineral abbreviations  
701 according to Whitney & Evans (2010). Qz: Quartz, Ms: Muscovite, Fsp: Feldspar, Chl: Chlorite, Pg:  
702 paragonite, C/S: chlorite-smectite mixed layers, Cel: celadonite, Prl: pyrophyllite, Cli+Daph:  
703 clinocllore + daphnite, Am: amesite, Sud: sudoite, Std Dv: standard deviation.

704 **Table 2.** Summary of the tectonometamorphic Variscan evolution of the Pulo do Lobo belt.

705

706

707 **References**

708 Abad, I., Mata, M.P., Nieto, F., and Velilla, N: The phyllosilicates in diagenetic-metamorphic rocks  
709 of the South Portuguese Zone, southwestern Portugal, *The Canadian Mineralogist*, 39(6),  
710 1571-1589, 2001.

711 Abad, I., Nieto, F., and Velilla, N.: Chemical and textural characterisation of diagenetic to low-grade  
712 metamorphic phyllosilicates in turbidite sandstones of the South Portuguese Zone: A  
713 comparison between metapelites and sandstones, *Schweizerische Mineralogische und*  
714 *Petrographische Mitteilungen*, 82(2), 303-324. 2002.

715 Abad, I., Nieto, F., and Gutiérrez-Alonso, G.: Textural and chemical changes in slate-forming  
716 phyllosilicates across the external-internal zones transition in the low-grade metamorphic  
717 belt of the NW Iberian Variscan Chain, *Swiss Bulletin of Mineralogy and Petrology*, 83(1),  
718 63-80, 2003a.

719 Abad, I., Gutierrez-Alonso, G., Nieto, F., Gertner, I., Becker, A., and Cabero, A.: The structure and  
720 the phyllosilicates (chemistry, crystallinity and texture) of Talas Ala-Tau (Tien Shan, Kyrgyz  
721 Republic); comparison with more recent subduction complexes, *Tectonophysics*, 365(1-4),  
722 103-127, 2003b.

723 Abad, I., Nieto, F., Velilla, N., and Suárez-Ruiz, I.: Metamorphic evidences from the Monchique  
724 pluton (South Portugal): Contact metamorphism vs regional metamorphism under very low-  
725 grade conditions, *Revista de la Sociedad Geológica de España*, 27(1): 337-350, 2014.

726 Abalos, B., Gil Ibarra, J.I., and Eguluz, L.: Cadomian subduction/collision and Variscan  
727 transpression in the Badajoz-Córdoba shear belt, southwest Spain, *Tectonophysics*, 199, 51-  
728 72, 1991.

729 Airaghi, L., Lanari, P., de Sigoyer, J., and Guillot, S.: Microstructural vs compositional preservation  
730 and pseudomorphic replacement of muscovite in deformed metapelites from the Longmen  
731 Shan (Sichuan, China), *Lithos*, 282, 262-280, 2017.

732 Ali, A.: The tectono-metamorphic evolution of the Balcooma Metamorphic Group, north-eastern  
733 Australia: a multidisciplinary approach, *Journal of Metamorphic Geology*, 28(4), 397-422,  
734 2010.

735 Apalategui, O., Barranco, E., Contreras, F., Delgado, M., and Roldán, F. J.: Hoja 916, Aroche, Mapa  
736 Geológico de España a escala 1:50000, Inst. Geológico y Minero de España, Madrid, 1983.

737 Araújo, A., Fonseca, P., Munhá, J., Moita, P., Pedro, J., and Ribeiro, A.: The Moura Phyllonitic  
738 Complex: an accretionary complex related with obduction in the southern Iberia Variscan  
739 suture, *Geodinamica Acta*, 18, 375-388, 2005.





- 740 Arenas, R., Abati, J., Martínez Catalán, J.R., García, F. D., and Pascual, F.R.: PT evolution of eclogites  
741 from the Agualada Unit (Ordenes Complex, northwest Iberian Massif, Spain): Implications  
742 for crustal subduction, *Lithos*, 40(2), 221-242, 1997.
- 743 Azor, A., González Lodeiro, F., and Simancas, J.F.: Tectonic evolution of the boundary between the  
744 Central Iberian and Ossa-Morena zones (Variscan Belt, southwest Spain), *Tectonics*, 13, 45-  
745 61, 1994.
- 746 Azor, A., Rubatto, D., Simancas, J.F., González Lodeiro, F., Martínez Poyatos, D., Martín Parra L.M.,  
747 and Matas, J.: Rheic Ocean ophiolitic remnants in Southern Iberia questioned by SHRIMP  
748 U-Pb zircon ages on the Beja-Acebuches amphibolites, *Tectonics*, 27(5), 2008.
- 749 Azor, A., Simancas, J.F., Martínez Poyatos, D., Pérez-Cáceres, I., González Lodeiro, F., and Expósito,  
750 I.: Chapter 10.3: Deformation and Structure, Southwestern Iberia, in: *The Geology of Iberia:  
751 A Geodynamic Approach, Volume 2: The Variscan Cycle*, edited by: Quesada, C., and  
752 Oliveira, J.T., Springer, 316-335, 2019.
- 753 Barbero, L.: Granulite-facies metamorphism in the Anatectic Complex of Toledo, Spain: late  
754 Hercynian tectonic evolution by crustal extension, *Journal of the Geological Society*, 152(2),  
755 365-382, 1995.
- 756 Bard, J.P.: Signification tectonique des métatholeites d'anité abyssale de la ceinture de base pression  
757 d'Aracena (Huelva, Espagne), *Bulletin de la Société Géologique de France*, 19, 385-393,  
758 1977.
- 759 Bastida, F., Martínez-Catalán, J.R., and Pulgar, J.A.: Structural, metamorphic and magmatic history  
760 of the Mondoñedo nappe (Hercynian belt, NW Spain). *Journal of Structural Geology*, 8(3-  
761 4), 415-430, 1986.
- 762 Bastida, F., Brime, C., García-López, S. Aller, J., Valin, M.L., and Sanz-López, J.: Tectono-thermal  
763 evolution of the Cantabrian Zone (NW Spain), in: *Palaeozoic conodonts from northern  
764 Spain*, edited by: García López, S., and Bastida, F., Instituto Geológico y Minero de España,  
765 Cuadernos del Museo Geominero, 1, 105-123, Madrid, ISBN: 84-7840-446-5, 2002.
- 766 Battaglia, S., Leoni, L., and Sartori, F.: The Kübler index in late diagenetic to low-grade metamorphic  
767 pelites: a critical comparison of data from 10 Å and 5 Å peaks, *Clays and Clay Minerals*,  
768 52(1), 85-105, 2004.
- 769 Beyssac, O., Goffé, B., Chopin, C., and Rouzaud, J.N.: Raman spectra of carbonaceous material in  
770 metasediments: a new geothermometer, *Journal of Metamorphic Geology*, 20, 859-871,  
771 2002a.
- 772 Beyssac, O., Rouzaud, J.-N., Goffé, B., Brunet, F., and Chopin, C.: Graphitization in a high-pressure,  
773 low temperature metamorphic gradient: a Raman microspectroscopy and HRTEM study.  
774 *Contrib. Mineral. Petrol.*, 143, 19-31, 2002b.
- 775 Beyssac, O., Goffé, B., Petit, J.P., Froigneux, E., and Rouzaud, J.N.: On the characterization of  
776 disordered and heterogeneous carbonaceous materials using Raman spectroscopy,  
777 *Spectrochim. Acta A Mol. Biomol. Spectrosc.*, 59, 2267-2276, 2003.
- 778 Beyssac, O., Bollinger, L., Avouac, J.P., and Goffé, B.: Thermal metamorphism in the lesser Himalaya  
779 of Nepal determined from Raman spectroscopy of carbonaceous material, *Earth and  
780 Planetary Science Letters*, 225, 233-241, 2004.
- 781 Booth-Rea, G., Simancas, J.F., Azor, A., Azañón, J.M., Gonzalez Lodeiro, F., and Fonseca, P.: HP-  
782 LT Variscan metamorphism in the Cubito-Moura schists (Ossa-Morena Zone, southern  
783 Iberia), *Comptes Rendus Geoscience*, 338(16), 1260-1267, 2006.



- 784 Bourdelle, F., Parra, T., Chopin, C., and Beyssac, O.: A new chlorite geothermometer for diagenetic  
785 to low-grade metamorphic conditions, *Contributions to Mineralogy and Petrology*, 165(4),  
786 723-735, 2013.
- 787 Bousquet, R., Oberha, R., Goffé, B., Wiederkehr, M., Koller, F., Schmid, S.M., Schuster, R., Engi,  
788 M., Berger, A., and Martinotti, G.: Metamorphism of metasediments at the scale of an  
789 orogen: a key to the tertiary geodynamic evolution of the Alps, Geological Society, London,  
790 Special Publications, 298, 393-411, 2008.
- 791 Braid, J.A., Murphy, J.B., and Quesada, C.: Structural analysis of an accretionary prism in a continental  
792 collisional setting, the Late Paleozoic Pulo do Lobo Zone, Southern Iberia, *Gondwana  
793 Research*, 17(2-3), 422-439, 2010.
- 794 Braid, J. A., Murphy, J. B., Quesada, C., and Mortensen, J.: Tectonic escape of a crustal fragment  
795 during the closure of the Rheic Ocean: U–Pb detrital zircon data from the Late Palaeozoic  
796 Pulo do Lobo and South Portuguese zones, southern Iberia, *Journal of the Geological  
797 Society*, 168(2), 383-392, 2011.
- 798 Brown, M.: P–T–t evolution of orogenic belts and the causes of regional metamorphism, *Journal of  
799 the Geological Society*, 150(2), 227-241, 1993.
- 800 Burg, J.P., Iglesias, M., Laurent, P., Matte, P., and Ribeiro, A.: Variscan intracontinental deformation:  
801 the Coimbra-Córdoba Shear zone (SW Iberian Peninsula), *Tectonophysics*, 78, 161-177,  
802 1981.
- 803 Cantarero, I., Lanari, P., Vidal, O., Alías, G., Travé, A., and Baqués, V.: Long-term fluid circulation  
804 in extensional faults in the central Catalan Coastal Ranges: P–T constraints from neofomed  
805 chlorite and K-white mica, *International Journal of Earth Sciences*, 103(1), 165-188, 2014.
- 806 Castro, A., Fernández, C., De la Rosa, J.D., Moreno Ventas, I., and Rogers, G.: Significance of  
807 MORB-derived amphibolites from the Aracena metamorphic belt, southwest Spain, *Journal  
808 of Petrology*, 37(2), 235-260, 1996.
- 809 Castro, A., Fernández, C., El-Hmidi, H., El-Biad, M., Díaz, M., De la Rosa, J., and Stuart, F.: Age  
810 constraints to the relationships between magmatism, metamorphism and tectonism in the  
811 Aracena metamorphic belt, southern Spain, *International Journal of Earth Sciences*, 88(1),  
812 26-37, 1999.
- 813 Cathelineau, M.: Cation site occupancy in chlorites and illites as a function of temperature, *Clay  
814 Minerals* 23, 471-485, 1988.
- 815 Cathelineau, M., and Nieva, D.: A chlorite solid solution geothermometer the Los Azufres (Mexico)  
816 geothermal system, *Contrib. Mineral Petrol.*, 91(3), 235-244, 1985.
- 817 Coggon, R., and Holland, T.J.B.: Mixing properties of phengitic micas and revised garnet-phengite  
818 thermobarometers, *Journal of Metamorphic Geology*, 20(7), 683-696, 2002.
- 819 Crespo-Blanc, A.: Evolución geotectónica del contacto entre la zona de Ossa-Morena y la zona  
820 Surportuguesa en las sierras de Aracena y Aroche (Macizo Ibérico Meridional): Un contacto  
821 mayor en la cadena Hercínica Europea, Ph.D. Thesis, Univ. de Granada, 327 pp., 1991.
- 822 Crouzet, C., Dunkl, I., Paudel, L., Arkai, P., Rainer, T.M., Balogh, K., and Appel, E.: Temperature  
823 and age constraints on the metamorphism of the Tethyan Himalaya in Central Nepal: A  
824 multidisciplinary approach, *Journal of Asian Earth Sciences*, 30(1), 113-130, 2007.
- 825 Dahn, D.R.L., Braid, J.A., Murphy, J.B., Quesada, C., Dupuis, N., and McFarlane C.R.M.:  
826 Geochemistry of the Peramora Melange and Pulo do Lobo schist: Geochemical investigation



- 827 and tectonic interpretation of mafic melange in the Pangean suture zone, Southern Iberia,  
828 *International Journal of Earth Sciences*, 103(5), 1415-1431, 2014.
- 829 Dallmeyer, R.D., Fonseca, P.E., Quesada, C., and Ribeiro, A.:  $^{40}\text{Ar}/^{39}\text{Ar}$  mineral age constraints for  
830 the tectonothermal evolution of a variscan suture in Southwest Iberia, *Tectonophysics*, 222,  
831 177-194, 1993.
- 832 De Andrade, V., Vidal, O., Lewin, E., O'Brien, P., and Agard, P.: Quantification of electron  
833 microprobe compositional maps of rock thin sections: an optimized method and examples,  
834 *Journal of Metamorphic Geology*, 24(7), 655-668, 2006.
- 835 Díaz Azpiroz, M., Fernández, C., Castro, A., and El-Biad, M.: Tectonometamorphic evolution of the  
836 Aracena metamorphic belt (SW Spain) resulting from ridge-trench interaction during  
837 Variscan plate convergence, *Tectonics*, 25(1), 2006.
- 838 Eden, C.P.: Tectonostratigraphic analysis of the northern extent of the oceanic exotic terrane,  
839 Northwestern Huelva Province, Spain, Ph. D. Thesis, Univ. of Southampton, 214 pp., 1991.
- 840 Eden, C., and Andrews, J.: Middle to upper Devonian melanges in SW Spain and their relationship  
841 to the Meneage formation in south Cornwall. *Proc. Ussher Soc.*, 7, 217-222, 1990.
- 842 Endo, S., and Wallis, S.R.: Structural architecture and low-grade metamorphism of the Mikabu-  
843 Northern Chichibu accretionary wedge, SW Japan, *Journal of Metamorphic Geology*, 35(6),  
844 695-716, 2017.
- 845 Ernst, W.G.: Tectonic history of subduction zones inferred from retrograde blueschist PT paths,  
846 *Geology* 16(12), 1081-1084, 1988.
- 847 Ernst, W.G.: Alpine and Pacific styles of Phanerozoic mountain building: subduction-zone  
848 petrogenesis of continental crust, *Terra Nova*, 17(2), 165-188, 2005.
- 849 Escuder Viruete, J., Arenas, R., and Martínez Catalán, J.R.: Tectonothermal evolution associated with  
850 Variscan crustal extension in the Tormes gneiss dome (NW Salamanca, Iberian Massif,  
851 Spain), *Tectonophysics*, 238(1-4), 117-138, 1994.
- 852 Fonseca, P., and Ribeiro, A.: Tectonics of the Beja-Acebuches ophiolite - a major suture in the Iberian  
853 variscan foldbelt, *Geol. Rundsch.*, 82, 440-447, 1993.
- 854 Fonseca, P., Munhá, J., Pedro, J., Rosas, F., Moita, P., Araujo, A., and Leal, N.: Variscan ophiolites  
855 and high-pressure metamorphism in southern Iberia. *Ophioliti*, 24, 259-268, 1999.
- 856 Franceschelli, M., Leoni, L., Memmi, I., and Puxeddu, M.: Regional distribution of Al-silicates and  
857 metamorphic zonation in the low-grade Verrucano metasediments from the Northern  
858 Apennines, Italy, *Journal of Metamorphic Geology*, 4(3), 309-321, 1986.
- 859 Frey, M.: Very low-grade metamorphism of clastic sedimentary rocks, in: *Low temperature  
860 metamorphism*, edited by: Frey, M., Blackie, Glasgow, 9-58, 1987.
- 861 Frey, M., and Robinson, D.: *Low-Grade Metamorphism*, 313 pp. Blackwell Science Ltd, Cambridge,  
862 1999.
- 863 Gil Ibarguchi, J., Mendia, M., Girardeau, J., and Peucat, J.J.: Petrology of eclogites and clinopyroxene-  
864 garnet metabasites from the Cabo Ortegal Complex (northwestern Spain), *Lithos*, 25(1-3),  
865 133-162, 1990.
- 866 Goffé, B., and Velde, B.: Contrasted metamorphic evolutions in thrustured cover units of the  
867 Briançonnais zone (French Alps): A model for the conservation of HP-LT metamorphic  
868 mineral assemblages, *Earth and Planetary Science Letters*, 68(2), 351-360, 1984.



- 869 Grosch, E.G., Vidal, O., Abu-Alam, T., and McLoughlin, N.: P–T constraints on the metamorphic  
870 evolution of the Paleoproterozoic Kromberg type-section, Barberton greenstone belt, South  
871 Africa, *Journal of Petrology*, 53(3), 513–545, 2012.
- 872 Grosch, E.G., McLoughlin, N., Lanari, P., Erambert, M., and Vidal, O.: Microscale mapping of  
873 alteration conditions and potential biosignatures in basaltic-ultramafic rocks on early Earth  
874 and beyond, *Astrobiology*, 14(3), 216–228, 2014.
- 875 Guidotti, C.V., and Sassi, F.P.: Classification and correlation of metamorphic facies series by means  
876 of muscovite b data from low-grade metapelites, *Neues Jahrbuch für Mineralogie-  
877 Abhandlungen*, 153, 363–380, 1986.
- 878 Guidotti, C. V., Mazzoli, C., Sassi, F. P., and Blencoe, J. G.: Compositional controls on the cell  
879 dimensions of 2M 1 muscovite and paragonite, *European Journal of Mineralogy*, 4(2), 283–  
880 297, 1992.
- 881 Guidotti, C.V., Sassi, F.P., Blencoe, J.G., and Selverstone, J.: The paragonite–muscovite solvus: I. P-  
882 T–X limits derived from the Na – K compositions of natural, quasibinary paragonite-  
883 muscovite pairs, *Geoch. Cosmochim. Acta*, 58, 2269–2275, 1994.
- 884 Gutiérrez-Alonso, G., and Nieto, F.: White-mica 'crystallinity', finite strain and cleavage development  
885 across a large Variscan structure, NW Spain, *Journal of the Geological Society*, 153(2), 287–  
886 299, 1996.
- 887 Hilchie, L.J., and Jamieson, R.A.: Graphite thermometry in a low-pressure contact aureole, Halifax,  
888 Nova Scotia, *Lithos*, 208, 21–33, 2014.
- 889 Jarosewich, E.J., Nelen, J.A., and Norberg, J.A.: Reference samples for electron microprobe analysis:  
890 *Geostandards Newsletter*, 4, 43–47, 1980.
- 891 Kisch, H.J.: Correlation between indicators of very low-grade metamorphism. In: *Low temperature  
892 metamorphism*, edited by: Frey, M., Blackie, Glasgow, 227–300, 1987.
- 893 Kisch, H.J.: Illite crystallinity: recommendations on sample preparation, X-ray diffraction settings,  
894 and interlaboratory samples, *Journal of Metamorphic Geology*, 9, 665–670, 1991.
- 895 Kübler, B. : Evaluation quantitative du métamorphisme par la cristallinité de l'illite. *Bull. Centres Rech.  
896 Pau-SNPA 2*, 385–397, 1968.
- 897 Lahfid, A., Beyssac, O., Deville, E., Negro, F., Chopin, C., and Goffé, B.: Evolution of the Raman  
898 spectrum of carbonaceous material in low-grade metasediments of the Glarus Alps  
899 (Switzerland), *Terra Nova*, 22, 354–360, 2010.
- 900 Lanari, P., Guillot, S., Schwartz, S., Vidal, O., Tricart, P., Riel, N., and Beyssac, O. : Diachronous  
901 evolution of the alpine continental subduction wedge: evidence from P–T estimates in the  
902 Briançonnais Zone houillère (France–Western Alps), *Journal of Geodynamics*, 56–57, 39–54,  
903 2012.
- 904 Lanari, P., Vidal, O., de Andrade, V., Dubacq, B., Lewin, E., Grosch, E.G., and Schwartz, S.:  
905 XMapTools: A MATLAB©-based program for electron microprobe X-Ray image  
906 processing and geothermobarometry, *Computers & Geosciences*, 62, 227–240, 2014a.
- 907 Lanari, P., Rolland, Y., Schwartz, S., Vidal, O., Guillot, S., Tricart, P., and Dumont, T.: P–T–t  
908 estimation of deformation in low-grade quartz-feldspar-bearing rocks using thermodynamic  
909 modelling and <sup>40</sup>Ar/<sup>39</sup>Ar dating techniques: example of the Plan-de-Phasy shear zone unit  
910 (Briançonnais Zone, Western Alps), *Terra Nova*, 26(2), 130–138, 2014b.



- 911 Lopes, G., Pereira, Z., Fernandes, P., Wicander, R., Matos, J.X., Rosa, D., and Oliveira, J.T.: The  
912 significance of reworked palynomorphs (middle Cambrian to Tournaisian) in the Viséan  
913 Toca da Moura Complex (South Portugal). Implications for the geodynamic evolution of  
914 Ossa Morena Zone, *Rev. Palaeobot. Palynol.*, 200, 1-23, 2014.
- 915 López-Carmona, A., Pitra, P., and Abati, J.: Blueschist-facies metapelites from the Malpica-Tui Unit  
916 (NW Iberian Massif): phase equilibria modelling and H<sub>2</sub>O and Fe<sub>2</sub>O<sub>3</sub> influence in high-  
917 pressure assemblages, *Journal of Metamorphic Geology*, 31(3), 263-280, 2013.
- 918 López Munguira, A., Nieto, F., Pardo, E. S., and Velilla, N.: The composition of phyllosilicates in  
919 Precambrian, low-grade metamorphic, clastic rocks from the Southern Hesperian Massif  
920 (Spain) used as an indicator to metamorphic conditions, *Precambrian Research*, 53(3-4), 267-  
921 279, 1991.
- 922 López Sánchez-Vizcaíno, V., Gómez Pugnnaire, M.T., Azor, A., and Fernández Soler, J.M.: Phase  
923 diagram sections applied to amphibolites: a case study from the Ossa-Morena/Central  
924 Iberian Variscan suture (Southwestern Iberian Massif), *Lithos*, 68, 1-21, 2003.
- 925 Martínez Catalán, J.R.: Estratigrafía y estructura del Domo de Lugo (Sector Oeste de la Zona  
926 Asturoccidental-leonesa), *Corpus Geol. Gallaeciae (2º Serie)*, 2, 1-291, 1985.
- 927 Martínez Catalán, J.R., Rubio Pascual, F.J., Díez Montes, A., Díez Fernández, R., Gómez Barreiro,  
928 J., Dias Da Silva, Í., González Clavijo, E., Ayarza, P., and Alcock, J.E.: The late Variscan  
929 HT/LP metamorphic event in NW and Central Iberia: relationships to crustal thickening,  
930 extension, orocline development and crustal evolution, *Geological Society, London, Special  
931 Publications*, 405(1), 225-247, 2014.
- 932 Martínez Poyatos, D., Nieto, F., Azor, A., and Simancas, J.F.: Relationships between very low-grade  
933 metamorphism and tectonic deformation: Examples from the southern Central Iberian Zone  
934 (Iberian Massif, Variscan Belt), *Journal of the Geological Society*, 158, 953-968, 2001.
- 935 Martínez Poza, A.I., Martínez Poyatos, D., Simancas, J.F., and Azor, A.: La estructura varisca de la  
936 Unidad del Pulo do Lobo (SO del Macizo Ibérico) en las transversales de Aroche y Rosal de  
937 la Frontera (Huelva), *Geogaceta*, 52, 21-24, 2012.
- 938 Massonne, H.J., and Schreyer, W.: Phengite geobarometry based on the limiting assemblage with K-  
939 feldspar, phlogopite, and quartz, *Contributions to Mineralogy and Petrology*, 96, 212-224,  
940 1987.
- 941 Massonne, H.J., and Szpurka, Z.: Thermodynamic properties of white micas on the basis of high-  
942 pressure experiments in the systems K<sub>2</sub>O-MgO-Al<sub>2</sub>O<sub>3</sub>-SiO<sub>2</sub>-H<sub>2</sub>O and K<sub>2</sub>O-FeO-Al<sub>2</sub>O<sub>3</sub>-  
943 SiO<sub>2</sub>-H<sub>2</sub>O. *Lithos*, 41, 229-250, 1997.
- 944 Matte, P.: The Variscan collage and orogeny (480-290 Ma) and the tectonic definition of the Armorica  
945 microplate: A review, *Terra Nova*, 13, 122-128, 2001.
- 946 Merriman, R.J., and Frey, M.: Patterns of very low-grade metamorphism in metapelitic rocks, in: *Low-  
947 grade metamorphism*, edited by: Frey, M., and Robinson, D., Blackwell, Oxford, 61-107,  
948 1999.
- 949 Moita, P., Munhá, J., Fonseca, P., Pedro, J., Araújo, A., Tassinari, C., and Palacios, T.: Phase equilibria  
950 and geochronology of Ossa-Morena eclogites, *Actas do XIV Semana de Gequímica/VIII  
951 Congresso de gequímica dos Países de Língua Portuguesa*, 2, 471-474, 2005.
- 952 Moore, D.M., and Reynolds, R.C. Jr.: *X-ray Diffraction and the Identification and Analysis of Clay  
953 Minerals*, 2nd edition, Oxford University Press, Oxford, 1997.



- 954 Mori, H., Mori, N., Wallis, S., Westaway, R., and Annen, C.: The importance of heating duration for  
955 Raman CM thermometry: evidence from contact metamorphism around the Great Whin Sill  
956 intrusion, UK, *Journal of Metamorphic Geology*, 35(2), 165-180, 2017.
- 957 Munhá, J.: Metamorphic evolution of the south Portuguese/Pulo do Lobo zone, in: Pre-Mesozoic  
958 Geology of Iberia, edited by: Dallmeyer, R.D., and Martínez García, E., Springer, Berlin,  
959 Germany, pp. 363-368, 1990.
- 960 Nieto, F., and Sánchez-Navas, A.: A comparative XRD and TEM study of the physical meaning of  
961 the white mica «crystallinity» index, *European Journal of Mineralogy*, 6(5), 611-621, 1994.
- 962 Nieto, F., Mata, M.P., Bauluz, B., Giorgetti, G., Árkai, P., and Peacor, D.R.: Retrograde diagenesis, a  
963 widespread process on a regional scale, *Clay Minerals*, 40(1), 93-104, 2005.
- 964 Oliveira, J.T.: Part VI: South Portuguese Zone, stratigraphy and synsedimentary tectonism, in: Pre-  
965 Mesozoic Geology of Iberia, edited by: Dallmeyer, R.D., and Martínez García, E., Springer,  
966 Berlin, Germany, pp. 334-347, 1990
- 967 Olsson, I.: Regional burial heating vs. local magmatic heat influence of the Röstänga area, Scania,  
968 southern Sweden, *GFF*, 121(3), 209-214, 1999.
- 969 Omrani, H., Moazzen, M., Oberhänsli, R., and Moslempour, M.E.: Iranshahr blueschist: subduction  
970 of the inner Makran oceanic crust, *Journal of Metamorphic Geology*, 35(4), 373-392, 2017.
- 971 Ordóñez-Casado, B.: Geochronological studies of the Pre-Mesozoic basement of the Iberian Massif:  
972 the Ossa-Morena Zone and the Allochthonous Complexes within the Central Iberian Zone,  
973 Ph.D. Thesis, ETH Zurich, 235 pp., 1998.
- 974 Parra, T., Vidal, O., and Agard, P.: A thermodynamic model for Fe-Mg dioctahedral K White micas  
975 using data from phase-equilibrium experiments and natural pelitic assemblages, *Contrib.  
976 Mineral Petrol.*, 143, 706-732, 2002.
- 977 Pedro, J., Araujo, A., Fonseca, P., Tassinari, C., and Ribeiro, A.: Geochemistry and U-Pb Zircon Age  
978 of the Internal Ossa-Morena Zone Ophiolite Sequences: A Remnant of Rheic Ocean in SW  
979 Iberia, *Ofoliti*, 35(2), 117-130, 2010.
- 980 Pereira, M.F., Apraiz, A., Chichorro, M., Silva, J.B., and Armstrong, R.A.: Exhumation of high  
981 pressure rocks in northern Gondwana during the Early Carboniferous (Coimbra-Cordoba  
982 shear zone, SW Iberian Massif): tectonothermal analysis and U-Th-Pb SHRIMP in-situ  
983 zircon geochronology, *Gondwana Research*, 17, 440-460, 2010.
- 984 Pereira, M.F., Chichorro, M., Silva, J.B., Ordóñez-Casado, B., Lee, J.K., and Williams, I.S.: Early  
985 carboniferous wrenching, exhumation of high-grade metamorphic rocks and basin instability  
986 in SW Iberia: constraints derived from structural geology and U-Pb and <sup>40</sup>Ar-<sup>39</sup>Ar  
987 geochronology, *Tectonophysics*, 558, 28-44, 2012.
- 988 Pereira, M.F., Chichorro, M., Williams, I.S., Silva, J.B., Fernández, C., Díaz-Azpíroz, M., Apraiz, A.,  
989 and Castro, A.: Variscan intra-orogenic extensional tectonics in the Ossa-Morena Zone  
990 (Évora-Aracena-Lora del Río metamorphic belt, SW Iberian Massif): SHRIMP zircon U-Th-  
991 Pb geochronology, *Geological Society, London, Special Publications*, 327(1), 215-237, 2009.
- 992 Pereira, M.F., Martínez Poyatos, D., Pérez-Cáceres, I., Gama, C., and Azor, A.: Comment on  
993 “Stratigraphy of the Northern Pulo do Lobo Domain, SW Iberia Variscides: A palynological  
994 contribution” by Pereira, Z. et al. (2018) - *Geobios*, 51, 491-506. *Geobios*, in press, 2019.
- 995 Pereira, Z., Matos, J., Fernandes, P., and Oliveira, J.T.: Palynostratigraphy and systematic palynology  
996 of the Devonian and Carboniferous successions of the South Portuguese Zone, Portugal,





- 997 Memórias Geológicas do Instituto Nacional de Engenharia, Tecnologia e Inovação 34,  
998 Lisboa, 2008.
- 999 Pereira, Z., Fernandes, P., Matos, J., Jorge, R., and Oliveira, J.T.: Stratigraphy of the Northern Pulo  
1000 do Lobo Domain, SW Iberia Variscides: A palynological contribution, *Geobios*, 51, 491-506,  
1001 2018.
- 1002 Pérez-Cáceres, I., Martínez Poyatos, D., Simancas, J.F., and Azor, A.: The elusive nature of the Rheic  
1003 Ocean in SW Iberia, *Tectonics*, 34, 2429-2450, 2015.
- 1004 Pérez-Cáceres, I., Simancas, J.F., Martínez Poyatos, D., and Azor, A.: Oblique collision and  
1005 deformation partitioning in the SW Iberian Variscides, *Solid Earth*, 7, 857-872, 2016.
- 1006 Pérez-Cáceres, I., Martínez Poyatos, D., Simancas, J.F., and Azor, A.: Testing the Avalonian affinity  
1007 of the South Portuguese Zone and the Neoproterozoic evolution of SW Iberia through  
1008 detrital zircon populations, *Gondwana Research*, 42, 177-192, 2017.
- 1009 Petschick R.: [http://www.geol-pal.uni-frankfurt.de/  
1010 Staff/Homepages/Petschick/classicsoftware.html# MacDiff](http://www.geol-pal.uni-frankfurt.de/Staff/Homepages/Petschick/classicsoftware.html#MacDiff), 2004.
- 1011 Platt, J. P.: Dynamics of orogenic wedges and the uplift of high-pressure metamorphic rocks,  
1012 *Geological Society of America Bulletin*, 97(9), 1037-1053, 1986.
- 1013 Ponce, C., Simancas, J.F., Azor, A., Martínez Poyatos, D.J., Booth-Rea, G., and Expósito, I.:  
1014 Metamorphism and kinematics of the early deformation in the Variscan suture of SW Iberia,  
1015 *Journal of Metamorphic Geology*, 30(7), 625-638, 2012.
- 1016 Potel, S., Ferreiro-Mählmann, R., Stern, W. B., Mullis, J., and Frey, M.: Very low-grade metamorphic  
1017 evolution of pelitic rocks under high-pressure/low-temperature conditions, NW New  
1018 Caledonia (SW Pacific), *Journal of Petrology*, 47(5), 991-1015, 2006
- 1019 Potel, S., Maison, T., Maillet, M., Sarr, A. C., Doublier, M. P., Trullenque, G., and Mählmann, R. F.:  
1020 Reliability of very low-grade metamorphic methods to decipher basin evolution: Case study  
1021 from the Markstein basin (Southern Vosges, NE France), *Applied Clay Science*, 134, 175-  
1022 185, 2016.
- 1023 Quesada, C., Fonseca, P.E., Munhá, J., Oliveira, J.T., and Ribeiro, A.: The Beja-Acebuches Ophiolite  
1024 (Southern Iberia Variscan fold belt): geological characterization and significance, *Boletín  
1025 Geológico Minero*, 105, 3-49, 1994.
- 1026 Ribeiro, A., Munhá, J., Fonseca, P.E., Araujo, A., Pedro, J.C., Mateus, A., Tassinari, C., Machado, G.,  
1027 and Jesus, A.: Variscan ophiolite belts in the Ossa-Morena Zone (Southwest Iberia):  
1028 Geological characterization and geodynamic significance, *Gondwana Research*, 17(2-3), 408-  
1029 421, 2010.
- 1030 Rubio Pascual, F.J., Matas J., and Martín Parra, L.M.: High-pressure metamorphism in the Early  
1031 Variscan subduction complex of the SW Iberian Massif, *Tectonophysics*, 592, 187-199, 2013.
- 1032 Sassi, F.P., and Scolari, A.: The  $b_0$  value of the potassic white micas as a barometric indicator in low-  
1033 grade metamorphism of pelitic schists, *Contributions to Mineralogy and Petrology*, 45(2),  
1034 143-152, 1974.
- 1035 Silva, J. B., Oliveira, J.T., and Ribeiro, A.: South Portuguese Zone, structural outline, in: *Pre-  
1036 Mesozoic Geology of Iberia*, edited by: Dallmeyer, R.D., and Martínez García, E., Springer,  
1037 Berlin, Germany, pp. 348-362, 1990.
- 1038 Simancas, J.F., Carbonell, R., Lodeiro, F.G., Pérez-Estaún, A., Juhlin, C., Ayarza, P., Kashubin, A.,  
1039 Azor, A., Martínez Poyatos, D., Almodóvar, G.R., Pascual, E., Sáez, R., and Expósito, I.:





- 1040 Crustal structure of the transpressional Variscan orogen of SW Iberia: SW Iberia deep  
1041 seismic reflection profile (IBERSEIS), *Tectonics*, 22(6), 1062, 2003.
- 1042 Simancas, J.F., Expósito, I., Azor, A., Martínez Poyatos, D., and González Lodeiro, F.: From the  
1043 Cadomian orogenesis to the Early Palaeozoic Variscan rifting in Southwest Iberia, *Journal*  
1044 *of Iberian Geology*, 30, 53-71, 2004.
- 1045 Simancas, J.F., Carbonell, R., González Lodeiro, F., Pérez-Estaún, A., Juhlin, C., Ayarza, P.,  
1046 Kashubin, A., Azor A., Martínez Poyatos, D.J., Sáez, R., Almodóvar, G.R., Pascual R.,  
1047 Flecha, I., and Martí, D.: Transpressional collision tectonics and mantle plume dynamics:  
1048 The Variscides of southwestern Iberia, *Memoirs, Geol. Soc.*, 32(1), 345-354, 2006.
- 1049 Vázquez, M., Abad, I., Jiménez-Millán, J., Rocha, F.T., Fonseca, P.E., and Chaminé, H.I.: Prograde  
1050 epizonal clay mineral assemblages and retrograde alteration in tectonic basins controlled by  
1051 major strike-slip zones (W Iberian Variscan chain), *Clay Minerals*, 42(1), 109-128, 2007.
- 1052 Vidal, O., Parra, T., and Trotet, F.: A thermodynamic model for Fe-Mg aluminous chlorite using data  
1053 from phase equilibrium experiments and natural pelitic assemblages in the 100-600 °C 1-25  
1054 kbar range, *American Journal of Science*, 63, 557-592, 2001.
- 1055 Vidal, O., Parra, T., and Vieillard, P.: Thermodynamic properties of the Tschermak solid solution in  
1056 Fe-chlorite: application to natural examples and possible role of oxidation, *American*  
1057 *Mineralogist*, 90, 347-358, 2005.
- 1058 Vidal, O., de Andrade, V., Lewin, E., Muñoz, M., Parra, T., and Pascarelli, S.: P-T-deformation-  
1059 Fe<sup>3+</sup>/Fe<sup>2+</sup> mapping at the thin section scale and comparison with XANES mapping.  
1060 Application to a garnet-bearing metapelite from the Sambagawa metamorphic belt (Japan),  
1061 *Journal of Metamorphic Geology*, 24, 669-683, 2006.
- 1062 Vidal, O., Lanari, P., Munoz, M., Bourdelle, F., and De Andrade, V.: Deciphering temperature,  
1063 pressure and oxygen-activity conditions of chlorite formation, *Clay Minerals*, 51(4), 615-633,  
1064 2016.
- 1065 Warr, L.N., and Ferreiro Mählmann, R.: Recommendations for Kübler Index standardization, *Clay*  
1066 *Minerals*, 50(3), 283-286, 2015.
- 1067 Warr, L.N., and Rice, A.H.N.: Inter-laboratory standardization and calibration of clay mineral  
1068 crystallinity and crystallite size data, *Journal of Metamorphic Geology*, 12, 141-152, 1994.
- 1069 Whitney, D.L., and Evans, B.W.: Abbreviations for names of rock-forming minerals, *American*  
1070 *mineralogist*, 95(1), 185, 2010.



Figure 1

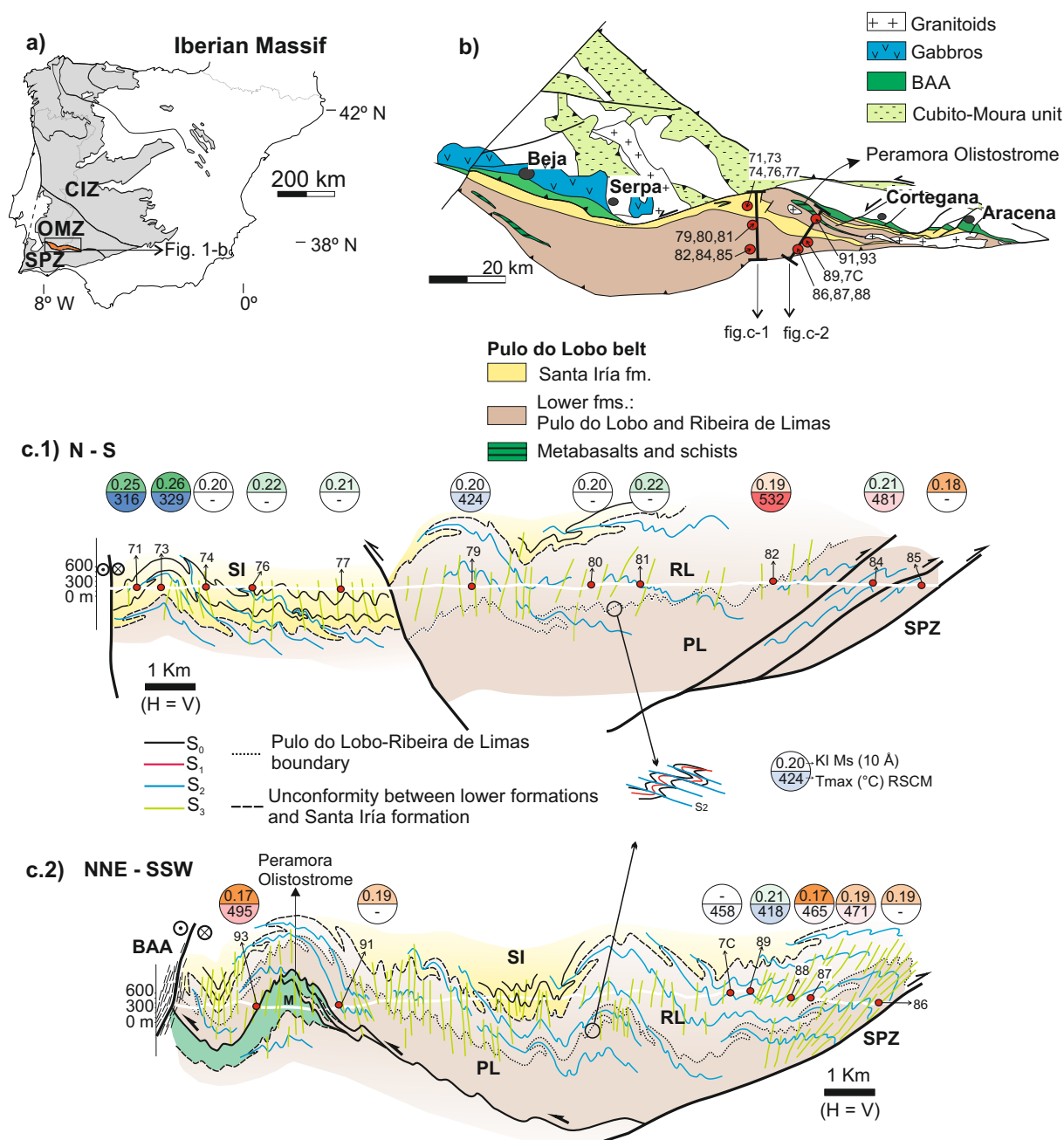






Figure 2

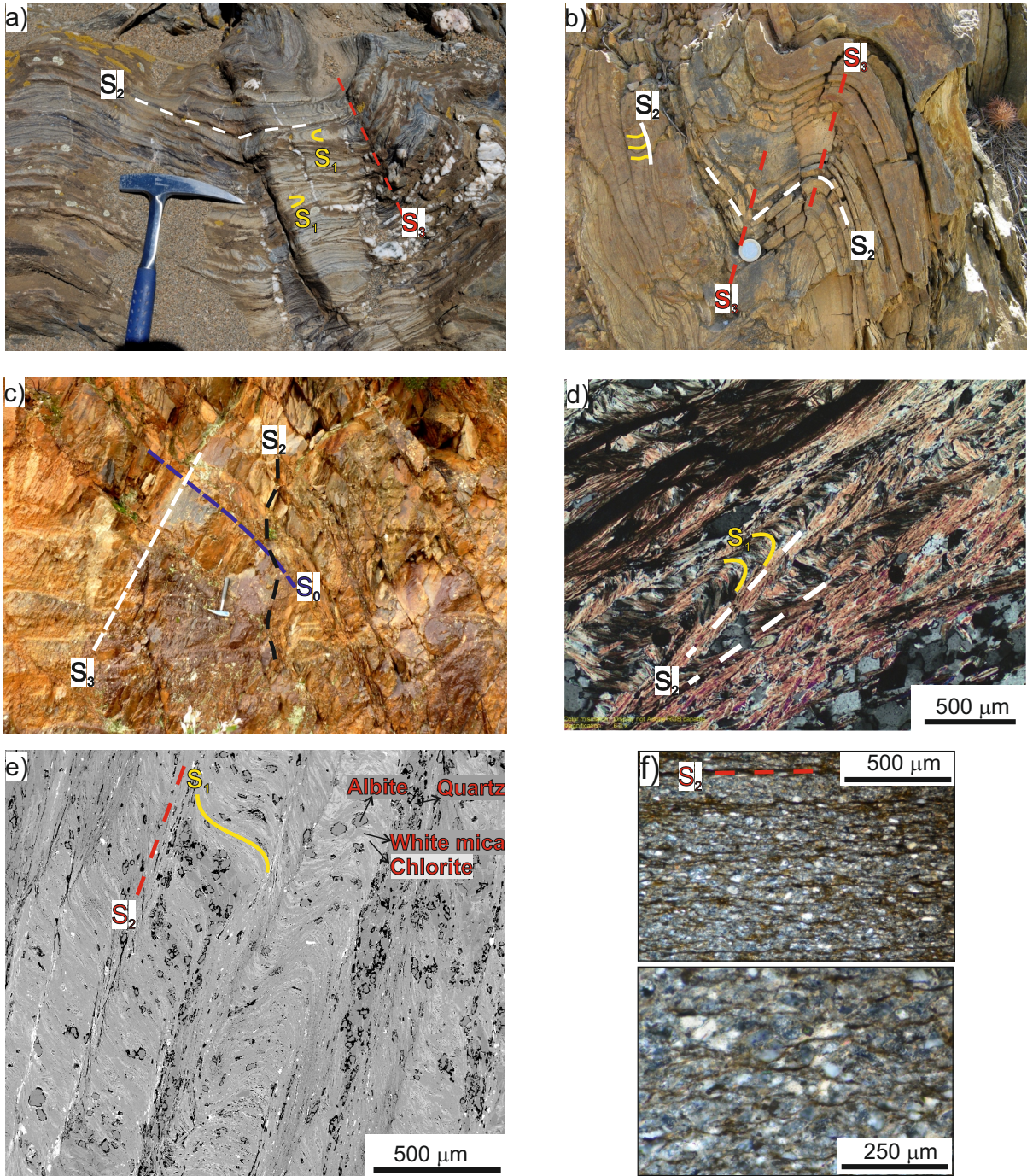




Figure 3

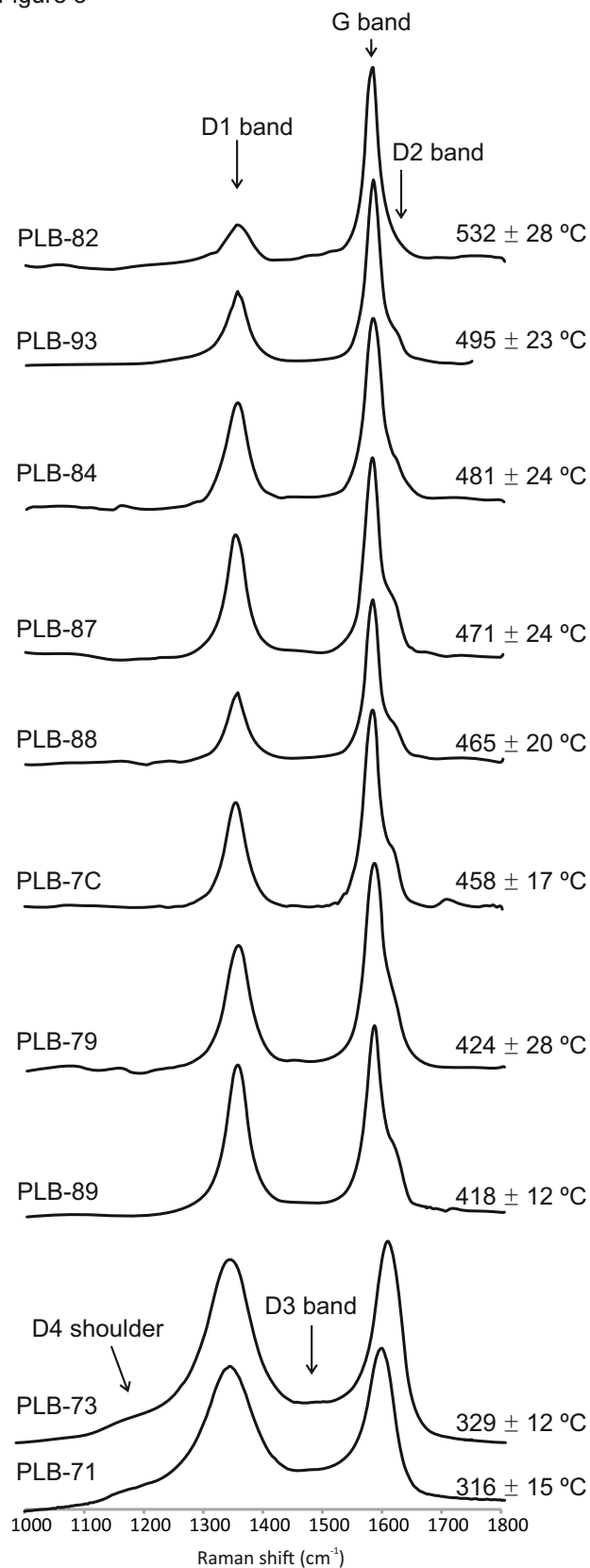






Figure 4

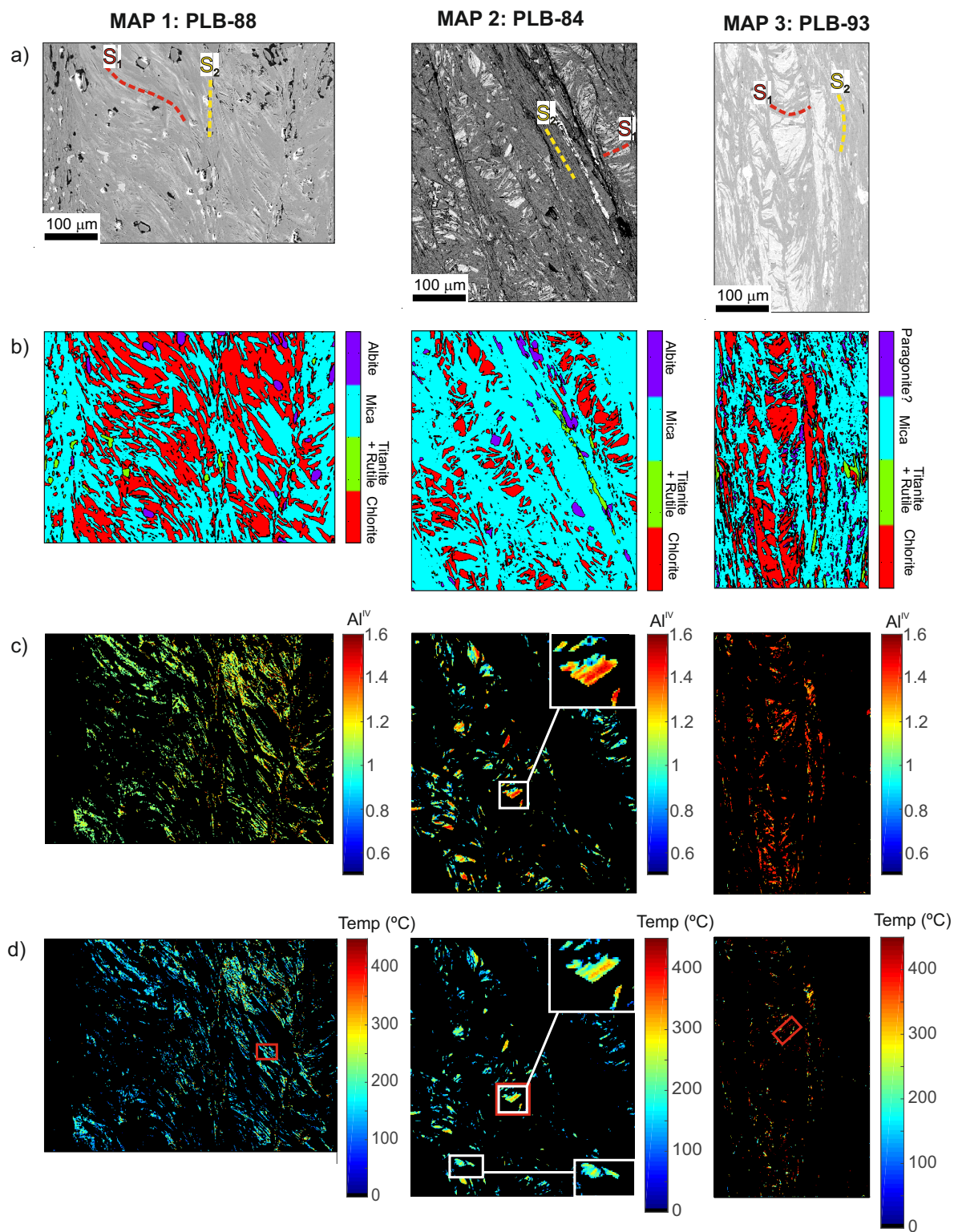




Figure 5

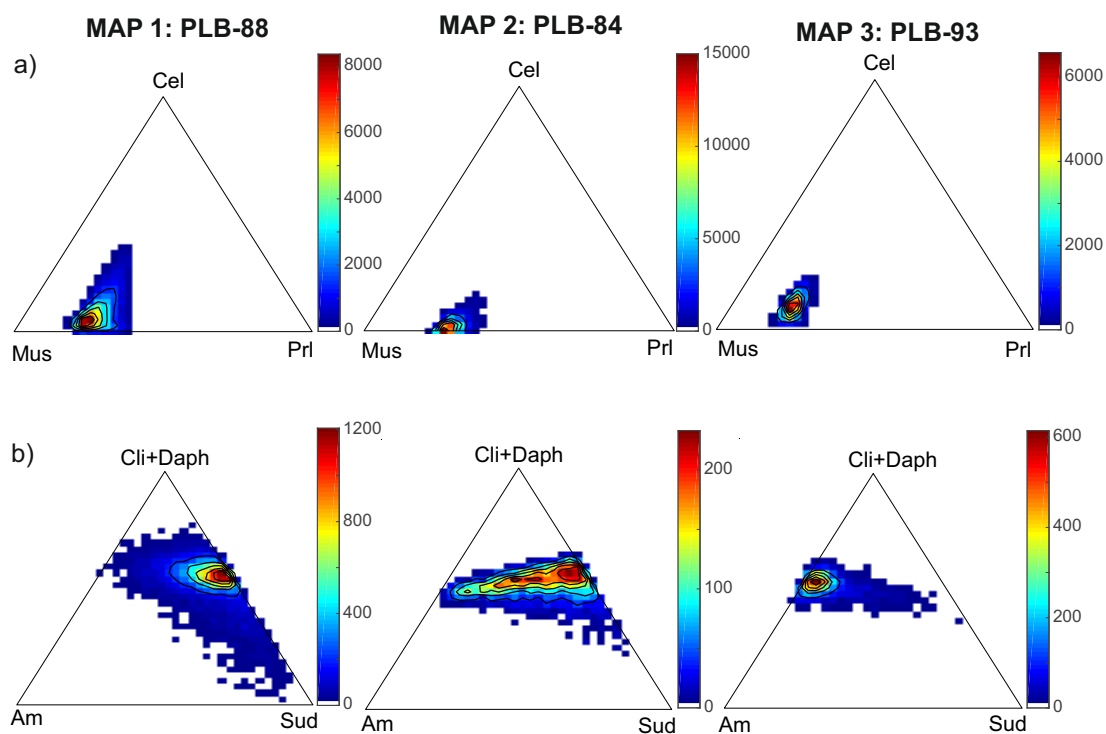
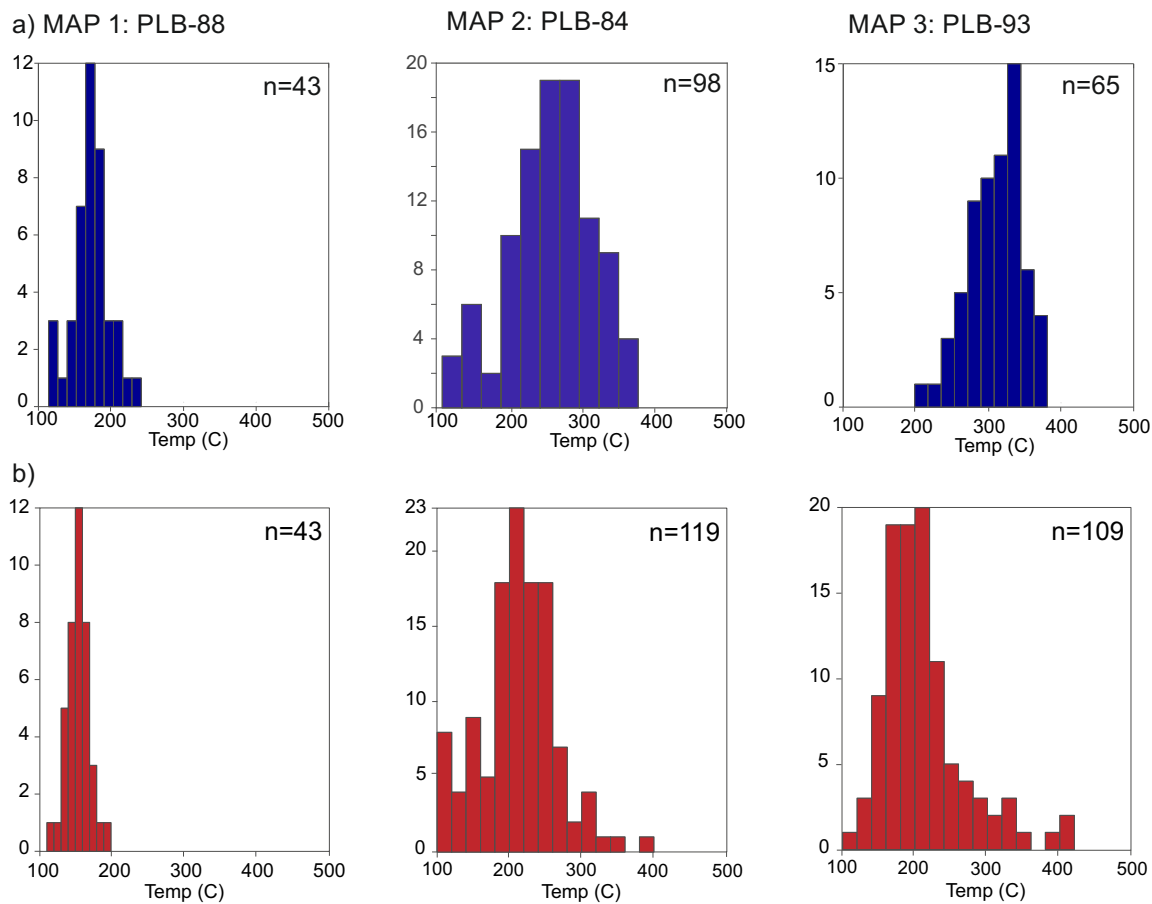








Figure 7





**Table 1**

Formation	Sample	Mineralogy	FWHM	Basel Kl (10 Å)		b (Å)	d <sub>001</sub> (Å)	White mica compositions			Chlorite compositions			Chlorite maps (Lanari et al., 2014b)	Chlorite thermometry		T <sub>max</sub> (°C) RSCM	
				bulk fraction	<2 µm			% Ms	% Ccl	% Pd	% CH+Daph	% Am	% Sud		T (°C)	T (°C)	Mean	Std Dv
Santa Iria (upper formation)	PLB-	Qz + Ms + Esp+	A			Ms	Ms											
	71	Chl	0.221	0.23	0.25	8.991	9.995	-	-	-	-	-	-	-	-	-	316	15
	73	Chl	0.227	0.22	0.26	8.996	9.997	-	-	-	-	-	-	-	-	-	329	12
	74	Chl + C/S	0.164	0.20	0.20	8.999	10.001	-	-	-	-	-	-	-	-	-	-	-
	76	Chl	0.184	0.20	0.22	8.997	9.997	-	-	-	-	-	-	-	-	-	-	-
	77	Chl + C/S	0.171	0.19	0.21	8.998	9.995	-	-	-	-	-	-	-	-	-	-	-
	79	Chl + Pg	0.17	0.18	0.20	8.995	9.993	-	-	-	-	-	-	-	-	-	424	28
	80	Chl	0.169	0.18	0.20	9.001	9.988	-	-	-	-	-	-	-	-	-	-	-
lower formations	81	Chl + Pg + C/S	0.181	0.19	0.22	-	9.988	-	-	-	-	-	-	-	-	-	-	-
	82	Chl + Pg	0.158	0.17	0.19	8.995	9.986	-	-	-	-	-	-	-	-	-	532	28
	84 (map 2)	Chl + Pg + C/S	0.173	0.17	0.21	8.994	9.988	70-80	0-10	20-30	50	0-50	0-50	150-350	150-375	150-350	481	24
	85	Chl + Pg	0.137	0.17	0.18	8.996	9.996	-	-	-	-	-	-	-	-	-	-	-
	86	Pg + C/S	0.144	0.18	0.19	8.993	9.986	-	-	-	-	-	-	-	-	-	-	-
	87	Chl + Pg	0.144	0.18	0.19	8.998	9.986	-	-	-	-	-	-	-	-	-	471	24
	88 (map 1)	Chl + Pg	0.129	0.18	0.17	8.997	9.99	70-80	0-10	20-30	50	0-10	20-50	100-200	120-230	150-200	465	20
	89	Chl	0.178	0.19	0.21	8.996	9.993	-	-	-	-	-	-	-	-	-	418	12
Santa Iria (lower formation)	91	Chl + Pg	0.143	0.17	0.19	9	9.995	-	-	-	-	-	-	-	-	-	-	-
	93 (map 3)	Chl + Pg	0.128	0.18	0.17	9.002	9.99	70-80	0-10	20-30	50	40-50	0-10	200-380	150-400	495	23	
	7C	-	-	-	8.993	-	-	-	-	-	-	-	-	-	-	458	17	



**Table 2**

Time	Deformation/metamorphic phase	Temperature	Low-grade metamorphic conditions
Middle-Upper Carboniferous	S <sub>3</sub> S <sub>2</sub> -M <sub>2</sub>	- <300 °C	- Epizone-Anchizone limit
Early Carboniferous (~340 Ma)	Beja-Acebuches and Pulo do Lobo metamafics Thermal imprint		
Upper Devonian	S <sub>1</sub> -M <sub>1</sub>	~300-450 °C	Epizone